Official journal of the CIOMP 2047-7538
www.nature.com/lsa

ARTICLE Open Access

Ultra-simplified diffraction-based computational spectrometer

Chuangchuang Chen[1], Honggang Gu[1,2]✉ and Shiyuan Liu[1,2]✉

Abstract

Miniaturizing spectrometers for compact and cost-effective mobile platforms is a major challenge in current spectroscopy research, where conventional spectrometers are impractical due to their bulky footprint. Existing miniaturized designs primarily rely on precalibrated response functions of nanophotonic structures to encode spectral information captured in a snapshot by detector arrays. Accurate spectrum reconstruction is achieved through computational techniques, but this requires precise component design, high-precision fabrication, and calibration. We propose an ultra-simplified computational spectrometer that employs a one-to-broadband diffraction decomposition strategy facilitated by a numerical regularized transform that depends only on the spectrum of the diffracted radiation. The key feature of our design is the use of a simple, arbitrarily shaped pinhole as the partial disperser, eliminating the need for complex encoding designs and full spectrum calibration. Our spectrometer achieves a reconstructed spectral peak location accuracy of better than 1 nm over a 200 nm bandwidth and excellent resolution for peaks separated by 3 nm in a bimodal spectrum, all within a compact footprint of under half an inch. Notably, our approach also reveals a breakthrough in broadband coherent diffractive imaging without requiring any *prior* knowledge of the broadband illumination spectrum, assumptions of non-dispersive specimens, or correction for detector quantum efficiency.

Introduction

Miniaturized spectrometers, characterized by their compact size and improved performance compared to conventional spectrometers, offer significant potential in various applications such as spectral characterization[1,2], materials analysis[3], and hyperspectral imaging[4]. Recent advancements in high-precision lithographic microfabrication[5] and computational techniques[6,7] have led to the development of a range of miniaturized spectrometers based on nanophotonic dispersive structures or spectral filter sensors. These spectrometers can be broadly categorized into two design approaches. The first approach involves one-to-one spectral-to-spatial mapping, where different bands of the light spectrum are separated spatially or temporally and then detected sequentially by a sensor array. Such spectrometers are generally based on conventional grating-based dispersions[8–11], meta-surface dispersions[12–15], waveguide propagations[16–18], digital planar holography[19,20], dispersive photonic crystals[21,22], narrowband filters[23–27], microfiber taper[28], and microcrystal resonators[29–32]. However, these instruments typically have limitations in terms of narrowband spectral dispersions across a wide spectrum range and suffer from low photon throughput. An alternative approach relies on broadband-to-broadband spectra mapping combined with computational retrieval algorithms. In this design, the intensities of multiple spectral bands are simultaneously detected after passing through different broadband filters, and the input spectrum is computationally reconstructed. Quantum dot arrays[33,34], nanowire sensors[35], and disordered multi-scatterings[36–38] have been explored in such designs. Nonetheless, the aforementioned systems require meticulous designs, and their performance is highly susceptible to fabrication errors and environmental disturbances. Complex calibration procedures and long-term

Correspondence: Honggang Gu (hongganggu@hust.edu.cn) or Shiyuan Liu (shyliu@hust.edu.cn)
[1]State Key Laboratory of Intelligent Manufacturing Equipment and Technology, Huazhong University of Science and Technology, Wuhan, Hubei 430074, China
[2]Optics Valley Laboratory, Wuhan, Hubei 430074, China

Table 1 Comparison of State-of-the-art Compact Computational Spectrometers

Method	Bandwidth ($\Delta\lambda/\lambda_c$)	Spectral resolution	Dispersion	Calibration	Architecture complexity
Nat. Photonics (2013)[37]	1%	0.75 nm	Photonic-crystal	Complex	Complex
Nature (2015)[33]	25%	3 nm	Quantum dots	Ultra-complex	Ultra-complex
Optica (2016)[36]	0.1%	0.01 nm	Multimode spiral	Complex	Ultra-complex
Science (2018)[14]	12%	NA	Metalens	Complex	Ultra-complex
Science (2019)[35]	10%	15 nm	Nanowire	Complex	Moderate
Nat. Photonics (2020)[53]	3.2%	10 nm	Nano-film	Moderate	Complex
Light Sci. Appl.(2021)[54]	35%	5.2 nm	Spectral camera	Ultra-complex	Ultra-complex
ACS Photonics (2022)[55]	3.4%	30 nm	Metalens	Complex	Complex
Light Sci. Appl.(2023)[15]	15%	22 nm	Metalens	Complex	Complex
eLight (2023)[28]	10%	6.89 pm	Microfiber taper	Ultra-complex	Simplified
This Work	28%	3 nm	Pinhole	Ultra-simplified	Ultra-simplified

*$\Delta\lambda$ = full width of the spectrum at half maximum, λ_c = center wavelength of the broadband spectrum

instability also limit the resolution and robustness of these methods. The representative state-of-the-art computational spectrometers over the past decade are summarized in Table 1.

Recently, broadband diffraction with partial coherence brought new insight into both coherent diffractive imaging (CDI)[39,40] and spectrum metrology[41,42]. This principle relies on the linear superposition of a broadband diffraction pattern, composed of coherent diffraction components that are inherently wavelength-dependent and characterized through the propagation of the spatial-spectral point-spread function (PSF) in the source spectrum. However, for diffraction-based spectrometers, the design of diffractive optics for encoding and the characterization of the PSF over the entire spectrum range requires careful calculations. These considerations introduce trade-offs that limit the performance of spectrometers in terms of simplicity and miniaturization.

Here, we report a novel and straightforward spectrometer design based on one-to-broadband diffraction mapping. Our innovative approach incorporates an arbitrarily shaped pinhole as a diffraction-based partial-disperser positioned in front of the detector. This eliminates the need for pre-encoding designs, making the spectrometer ultra-simplified. By solving a multi-variable linear equation (MLE), we can determine the incident light's spectrum accurately. The MLE is solved using coherent mode decomposition, employing a numerical regularized transform based on a single-shot measurement of quasi-monochromatic diffraction, which serves as the point-spread function (PSF). Importantly, the PSF relies solely on the diffracted radiation spectrum.

Experimental verification of our developed spectrometer demonstrates a reconstructed spectral peak location accuracy better than 1 nm over a 200 nm bandwidth and spectral resolution for a bimodal spectrum with peaks of 3 nm separation, all within a compact footprint of under half an inch. This represents the first demonstration of a spectrometer design that integrates an ultra-simplified and arbitrarily shaped diffraction structure. Our design eliminates the need for pre-encoding designs, high-precision fabrication, or complex calibration processes. It enables single-shot spectrum measurements across a wide wavelength range, from ultraviolet to infrared, with miniaturized lab-on-chip integration. This advancement is crucial for portable applications, offering high robustness, low cost, and long-term stability. Furthermore, the proposed method also reveals a significant breakthrough in broadband CDI without requiring any *prior* knowledge of the broadband illumination spectrum, assumptions of non-dispersive specimens, or correction of detector quantum efficiency (QE).

Results

Schematic of diffraction-based spectrometer

A diffraction pattern of a hollow microstructure (with a constant transmission over the whole concerned spectrum) with broadband radiation in an arbitrary state of coherence can be interpreted as a linear superposition of a discrete set of monochromatic diffraction patterns within the source spectrum. The diffraction intensity in each coherent mode is inherently wavelength-dependent and depends on the spectrum of the diffracted radiation[40]. It is possible to retrieve the spectrum from the broadband diffraction pattern with the knowledge of all spectral components of monochromatic diffractions, which can be treated as an ill-posed MLE. This means that the radiation spectrum could be calculated only if the transmittance coefficients of each

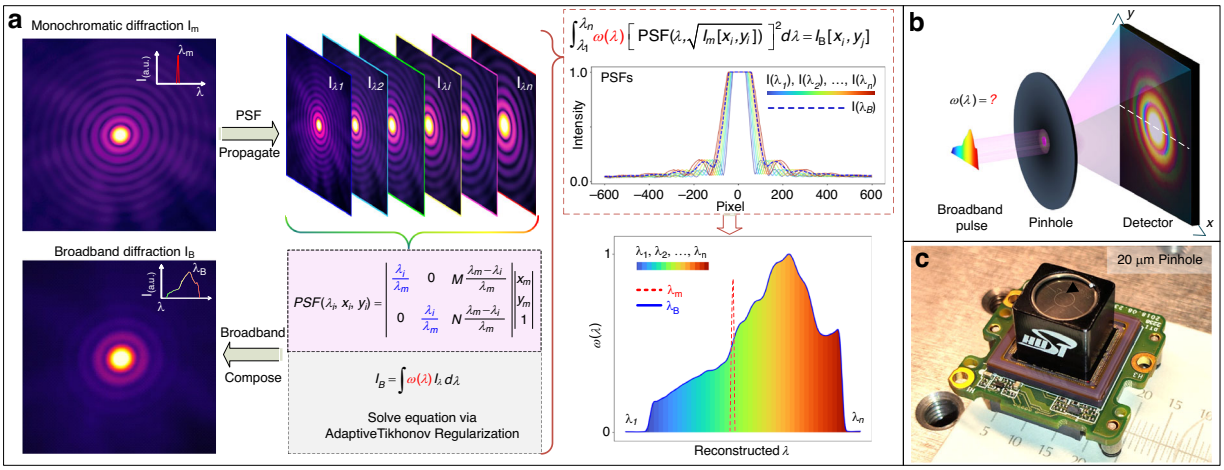

Fig. 1 The proposed one-to-broadband diffraction-based spectrometer. a Schematic of the operation principle from a monochromatic diffraction to a broadband diffraction, i.e., one-to-broadband diffraction. A broadband diffraction I_B captured in-situ can be represented as a superposition of wavelength-dependent PSFs from a single-shot monochromatic diffraction I_m at wavelength λ_m times the corresponding power spectrum components $\omega(\lambda)$ over full spectrum. The incident spectrum $\omega(\lambda)$ can be reconstructed using adaptive Tikhonov regularization. **b** Geometry of the proposed diffraction-based spectrometer. **c** A photograph of the ultra-compact computational spectrometer developed based on the proposed principle, which is integrated into a tiny CMOS panel (10 mm × 10 mm in size)

monochromatic diffraction for different wavelengths are pre-characterized as the encoding information. However, this calibration process is usually cumbersome, sometimes even not achievable in practical applications. The key point of our method is that each individual-wavelength diffraction profile I_λ at wavelength λ can be achieved from a single shot of a monochromatic diffraction pattern I_m at a given wavelength λ_m by utilizing the one-to-broadband PSF mapping scheme (Fig. 1a). Applied with this information, the input spectrum can be reconstructed from a single-shot broadband diffraction combined with its corresponding PSFs. For a given application in diffraction optics (Fig. 1b), a wave propagated from an object couples the amplitude and phase of a diffraction field $U(x', y', 0)$ through the Fraunhofer diffraction. Since the detector only records the amplitude of diffraction and drops the phase information, I_λ can be described as[43]:

$$I_\lambda(x,y,z) = \left(\frac{c}{\lambda z}\left|\mathcal{F}\{U(x',y',0)\}\right|_{u=\frac{x}{\lambda z}, v=\frac{y}{\lambda z}}\right)^2 \quad (1)$$

where propagation travels a distance of z, λ is the wavelength of the radiation and $\mathcal{F}$ denotes the 2D spatial Fourier transform of the sample $U(x', y', 0)$ at $z = 0$, with u and v the spatial frequencies. Equation (1) indicates that the Fraunhofer diffraction intensity distribution depends only on the propagation distance z and wavelength λ in an identical way, showing a wavelength-dependent scaling factor $c/\lambda z$, which allows us to map a coherent diffraction I_λ at an arbitrary wavelength from a single shot of monochromatic diffraction I_m at a given wavelength λ_m by PSF propagation between different spectral components (Fig. 1a). Owing to the microfeature size of the pinhole, the incident radiation can be considered as a spatial coherent illumination, which preserves a uniformity of the spectral intensity. Since the detector array captures a diffraction pattern with a much longer integration time than the coherence time of radiation, the broadband diffraction pattern I_B can be treated as the incoherent sum of all spectrum components, written as:

$$I_B = \int \omega(\lambda)[PSF(\lambda)]^2 d\lambda \quad (2)$$

where, $PSF(\lambda)$ represents the sum of PSFs from the reference diffraction I_m, and $\omega(\lambda)$ is the power spectrum of the diffracted light. Equation (2) indicates that a broadband diffraction pattern I_B captured by a detector with $M \times N$ pixels can be represented as the integral of $\omega(\lambda)[PSF(\lambda)]^2$ over the wavelength range, including of $M \times N$ multi-linear simultaneous equations with n variables of discrete spectral components over full spectrum range (details in Supplementary S1). Due to the measurement noise in both I_B and I_m combined with the approximation errors in PSF mapping that make the equations ill-posed, it is generally impossible to solve these equations straightforwardly by ordinary noniterative methods. Herein, a least-square-based multi-variable linear regression (MLR) scheme applying an adaptive Tikhonov regularization is employed to reconstruct the power spectrum $\omega(\lambda)$ and suppress the noises and errors during reconstruction. Additionally, generalized cross-validation (GCV) statistics are applied to balance the requirements of robustness and resolution[44] (details in Supplementary S2).

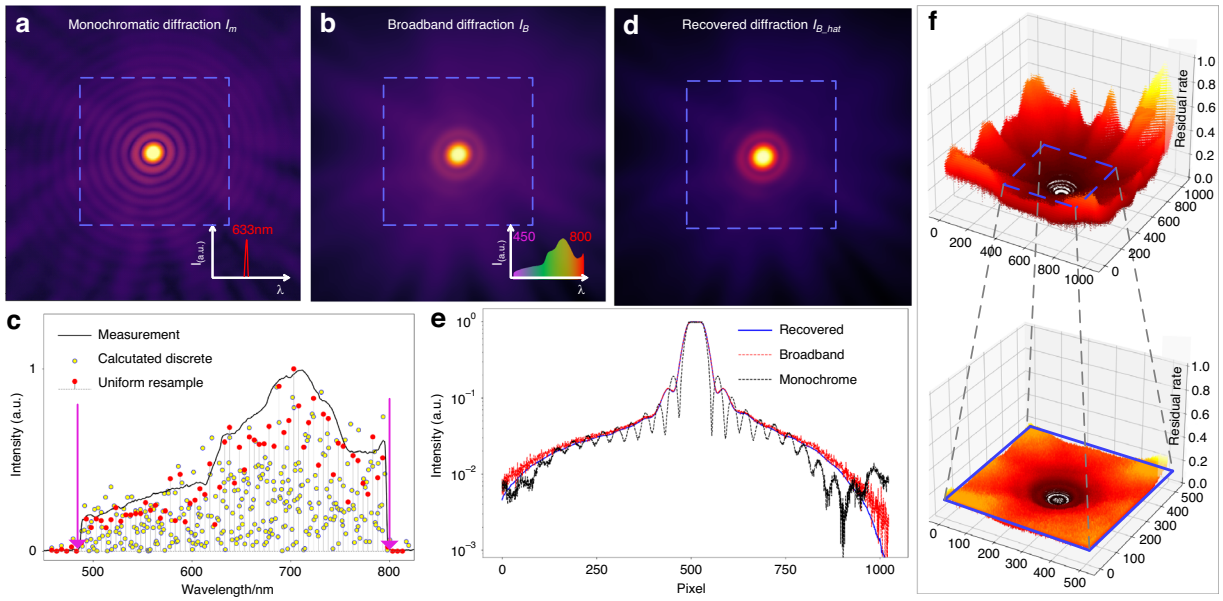

Fig. 2 Superposition of broadband diffraction via PSF mapping. a The coherent monochromatic diffraction I_m by a 633 nm band-filter. **b** The broadband diffraction I_B captured by a wide spectrum illumination. **c** The measured spectrum (solid curve), the calculated power spectrum components (yellow dots), and the linear fitting with a uniform interval of 5 nm (red dots). **d** Recovered diffraction I_{B_hat} from the calculated spectra power scatters. **e** Vertical line cuts along the center of the diffraction patterns, and red, black, and blue curves correspond to the patterns in subfigures **a**, **b**, and **ds**, respectively. **f** 3D distribution of an RR map between the measured diffraction I_B and its prediction I_{B_hat}, and the insert shows the zoom-in RR map in the region of blue boxes. All diffraction patterns are scaled to 1/2 power

Noting that the proposed one-to-broadband diffraction-based computational spectrometer is ultra-simplified and only relies on a single-shot of broadband diffraction I_B of an arbitrary shaped microstructure as input combined with a shot of monochromatic diffraction I_m pre-captured in situ without any movement parts or complex calibrations over full spectrum, it is designed with an ultra-compact form. As shown in Fig. 1c, the experimental prototype of such spectrometer was formed by coupling a Φ20 μm pinhole in front of the CMOS array detector. The system was integrated into a digital camera, with a size comparable footprint of 10 mm × 10 mm in size.

Experimental validation

To illustrate the performance of the proposed spectrometer, a group of experimental validations was performed using a supercontinuum light source (YSL Photonics SC-Pro-M) and a set of optical filters (Thorlabs F series) to modulate the shape of incident spectra. The light scattered from a Φ20 μm pinhole was recorded by a digital camera (MV-CA050) to capture a coherent quasi-monochromatic diffraction shot I_m from a narrowband spectrum and a broadband diffraction shot I_B in situ from an unknown wide spectrum, respectively (set-up detailed in Supplementary S3).

To verify the superposition of broadband diffraction via PSF mapping, we first captured a coherent monochromatic diffraction shot I_m (Fig. 2a) in situ at a 633 nm wavelength to generate a series of PSFs as the regressors over full band spectrum components and a shot of broadband diffraction I_B (Fig. 2b) from radiation with 350 nm bandwidth spectrum (Fig. 2c solid curve) as the spectrum-response variable. Then, 334 discrete counts of the power spectrum $\omega(\lambda)$ were calculated at different wavelength positions by solving Eq. (2) with the MLR scheme (Fig. 2c yellow dots). Then, a linear fitting with a uniform interval of 5 nm is processed to resample the calculated dataset (Fig. 2c red dots). Note that the distribution of the calculated power spectrum presents a high alignment with the measurement, even notably when subjected to specified step changes of the power spectrum. Thereafter, we recovered a prediction of the broadband diffraction I_{B_hat} by summing up the calculated spectral components times the corresponding PSFs (Fig. 2d). The recovered diffraction pattern matches well with the measured broadband diffraction, especially in the low orders of diffraction, while the intensities in high orders are blurred due to the inherent nature of temporal decoherence and the read noise of camera (Fig. 2e). Moreover, we used the residual rate (RR) $(I_B - I_{B\_hat})/I_B$ to evaluate the alignment between the captured broadband diffraction and its prediction (Fig. 2f). Seeing that the RR increases along with the order of the diffraction since only first several orders of broadband diffraction are

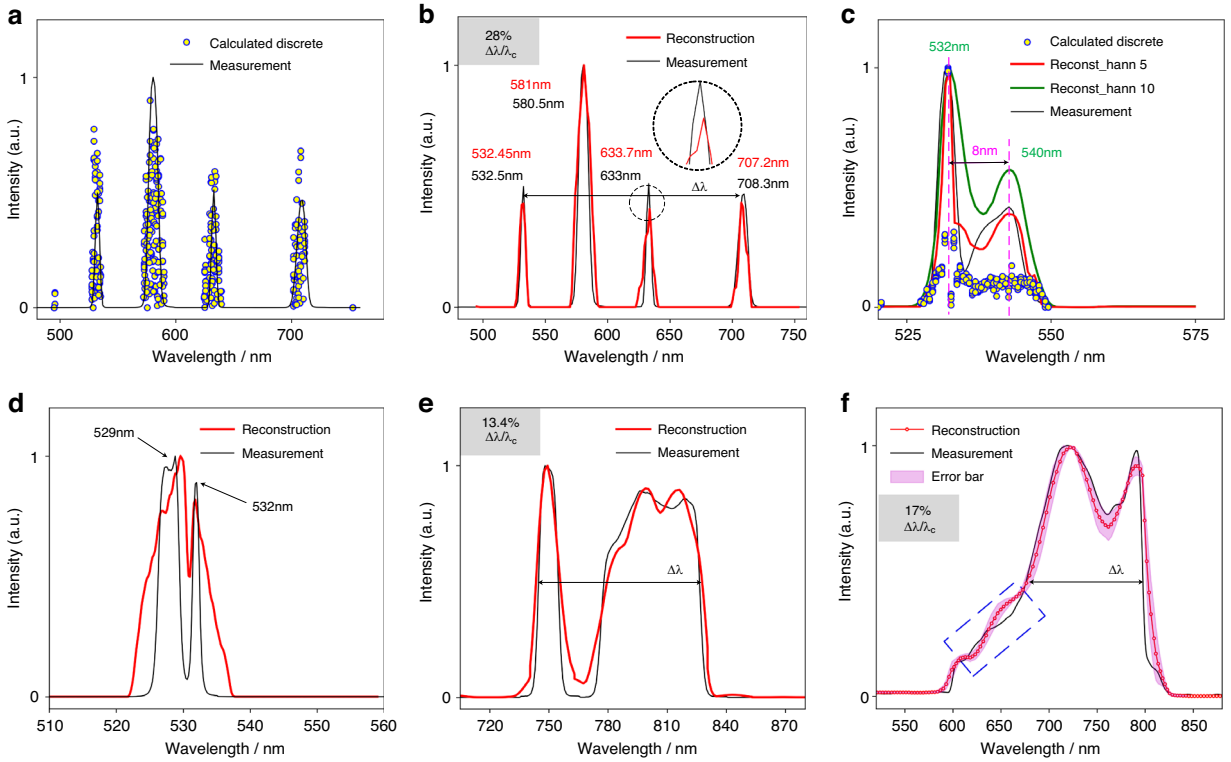

Fig. 3 Comparison between the reconstructed spectra (red curves) and the measurements (black curves) from a commercial grating-based spectrometer (Horiba iHR550). It should be noticed that all these results are normalized to their peak intensities and the QE coefficient of the detector is eliminated from the reconstructions. **a** Calculated discrete scatters (yellow circles) of a spectrum with 4 narrowband peaks corresponding to 532 nm, 580 nm, 633 nm, and 710 nm, compared with the measurement. **b** The reconstructed spectrum (red line) from the calculated discrete data in (**a**). **c** Calculated discrete scatters and the reconstructions of a bimodal spectrum with peaks of 8 nm apart under different Hann kernel sizes compared with the measurement. **d** The reconstruction of a bimodal spectrum with peaks of 3 nm separation. **e**, **f** Reconstructions of two different broadband spectra modulated by filters from a supercontinuum light source with the bandwidth of 100 nm and 230 nm, respectively. In **f**, the mean spectrum of five trials of measurements and the corresponding error bar (standard deviation)

recorded with high SNR (signal-to-noise ratio), corresponding to RR < 0.1.

Figure 3 presents five arbitrary spectra reconstructed by the above process (red curves) compared with the corresponding measurements (black curves). It should be mentioned that a quasi-monochromatic diffraction I_m from a given narrowband filter is pre-captured to generate the PSFs before each spectrum reconstruction, as mentioned above. Results in Fig. 3a were reconstructed from the corresponding pre-captured pattern I_m at the wavelength of 633 nm with a full width at half maximum (FWHM) of 3 nm, Fig. 3c, d from that at the wavelength of 532 nm with an FWHM of 3 nm and 1 nm, respectively, Fig. 3e from that at the wavelength of 750 nm with a FWHM of 10 nm, and Fig. 3f from that at the wavelength of 710 nm with a FWHM of 10 nm, respectively. In the first case, a wide spectrum with 4 narrowband peaks around the wavelength of 532 nm, 580 nm, 633 nm, and 710 nm was concerned, which was reconstructed from these calculated power spectrum components (Fig. 3a) via uniform resampling and convolution procedures. It indicates that the reconstructed spectrum exhibits a peak location accuracy better than 1 nm over the concerned 200 nm spectral range (Fig. 3b). In practice, the convolution with a Hann window is used to process the reconstructed spectrum, and the Hann kernel shapes the spectrum curves enormously (Fig. 3c), resulting in notable mismatch to the measurement in ground truth. It indicates that the convolution kernel should be carefully selected to improve the precision of spectrum reconstruction in practical applications. Furthermore, as illustrated in Fig. 3d, the proposed spectrometer presents a high spectral resolution and can easily distinguish a bimodal spectrum with peaks of 3 nm separation from the corresponding pre-captured narrowband diffraction with a FWHM of 1 nm. Moreover, to verify the robustness against the bandwidth, reconstructions of arbitrarily shaped broadband spectra with bandwidths of 100 nm and 230 nm were carried out, and results are respectively shown in Fig. 3e, f. Note that the reconstructed spectral

peaks agree well with the measurements in ground truth by a commercial grating-based spectrometer (Horiba iHR550), and the spectral curves are also well-traced with relatively low error bars. Tiny mismatches occur occasionally on steep turning points of the spectra when subjected to ultra-broadband spectrum, as indicated with the blue dashed box in Fig. 3f.

Spectrum reconstruction quality

The proposed one-to-broadband diffraction-based computational spectrometer is based on PSF mapping. Therefore, ideally, the spectral resolution is limited by the spectral sampling interval of the PSF mapping for a constant diffraction distance z:

$$\delta\lambda = \frac{{\lambda_m}^2}{(\lambda_1 + \lambda_n)n_{pixel}} \approx \frac{\lambda_m}{2n_{pixel}} \tag{3}$$

where n_{pixel} is the sum of pixels within the active sensor array size in the detector, λ_1 and λ_n denote the boundaries of the broadband spectrum. Equation (3) indicates that the spectral resolution is reciprocally related to the number of sampling pixels in the active detector sensor array, primarily determined by the detector's dynamic range. Since higher diffraction orders typically exhibit lower intensity, resulting in poor SNR. To address this, we intentionally overexpose and subsequently filter out the zero-order diffraction to fully utilize the sensor's dynamic range. Additionally, we eliminate background noise in the detector to enhance the diffraction SNR. In our diffraction-based spectrometer, utilizing larger active sensor arrays enhances spectrum measurement precision but also comes with a significant increase in computational expense. Consequently, we carefully bin the pixels to strike a balance between the quality of spectrum measurement and computational expenses. For a more detailed analysis, please refer to Supplementary S4.

In practical applications, the reconstructed spectrum is usually more sensitive to the diffraction efficiency of the disperser device. We further conducted two groups of validations by applying a Φ20 μm pinhole and a Φ100 μm Siemens star as the diffracted disperser, respectively. Noting that the diffractions from the Siemens star (Fig. 4b) retain more abundant information in frequency with high SNR than these from the pinhole (Fig. 4a), which can improve the generalization ability and the accuracy of the proposed diffraction-based computational spectrometer. here, we introduce the spectral correlation function of the PSF to determine the spectral resolution, as given by:

$$C(\delta\lambda) = \frac{\mathrm{cov}(PSF(\lambda_m), PSF(\lambda_m + \delta\lambda))}{\sigma(PSF(\lambda_m))\sigma(PSF(\lambda_m + \delta\lambda))} \tag{4}$$

Figure 4c plots the spectral correlation functions $C(\delta\lambda)$ of the PSFs for different pixel sizes and diffraction devices as a function of $\delta\lambda$ in wavelength space. Seeing that the spectral correlation functions of the Siemens star drop more steeply than those of the pinhole, the decrease in pixel size will also be helpful in reducing the spectral correlation function. Since the PSFs are performed as the regressors over the full spectral range in the proposed MLR scheme, that's to say, the lower the correlation of the PSFs, the more spectrum power components can be recovered. Experimental results shown in Fig. 4d, e provide evidence to support this point. Figure 4d comparatively shows the counts of the calculated spectrum components over 10 trails of calculations from the Siemens star and the pinhole, respectively. it can be observed that 180 discrete counts are calculated from the Siemens star, whereas only about 120 counts from the pinhole, which eventually results in a much more precise reconstructed spectrum for the Siemens star than that for the

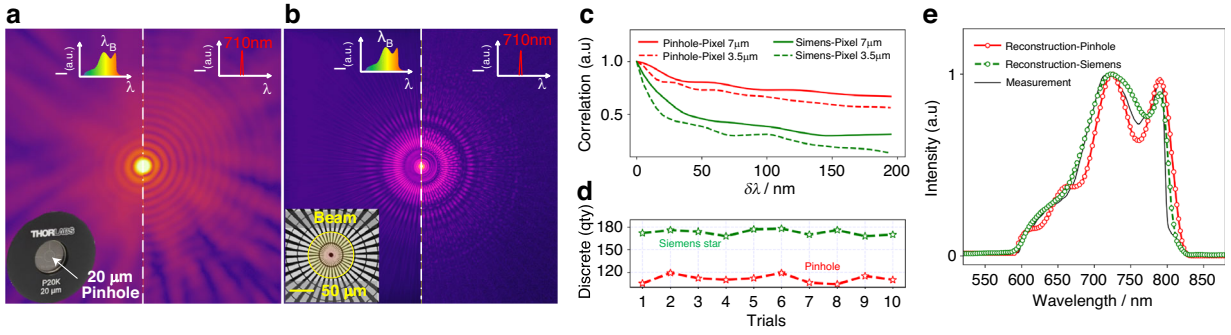

Fig. 4 Diffraction efficiency of the diffracted disperser boosts spectral measurement quality. a, **b** Broadband (left) and narrowband (right, wavelength of 710 nm with 10 nm FWHM) diffractions of a pinhole and a Siemens star, respectively. **c** The calculated spectral correlation function of the PSF for different diffraction devices and pixel sizes of the detector. **d** The counts of the calculated spectrum components over 10 trails of calculations from the diffraction data of the Siemens star and pinhole, respectively. **e** Reconstructed spectra for the Siemens star and the pinhole, corresponding to a pixel size of 7 μm, compared with the measurement (black curve)

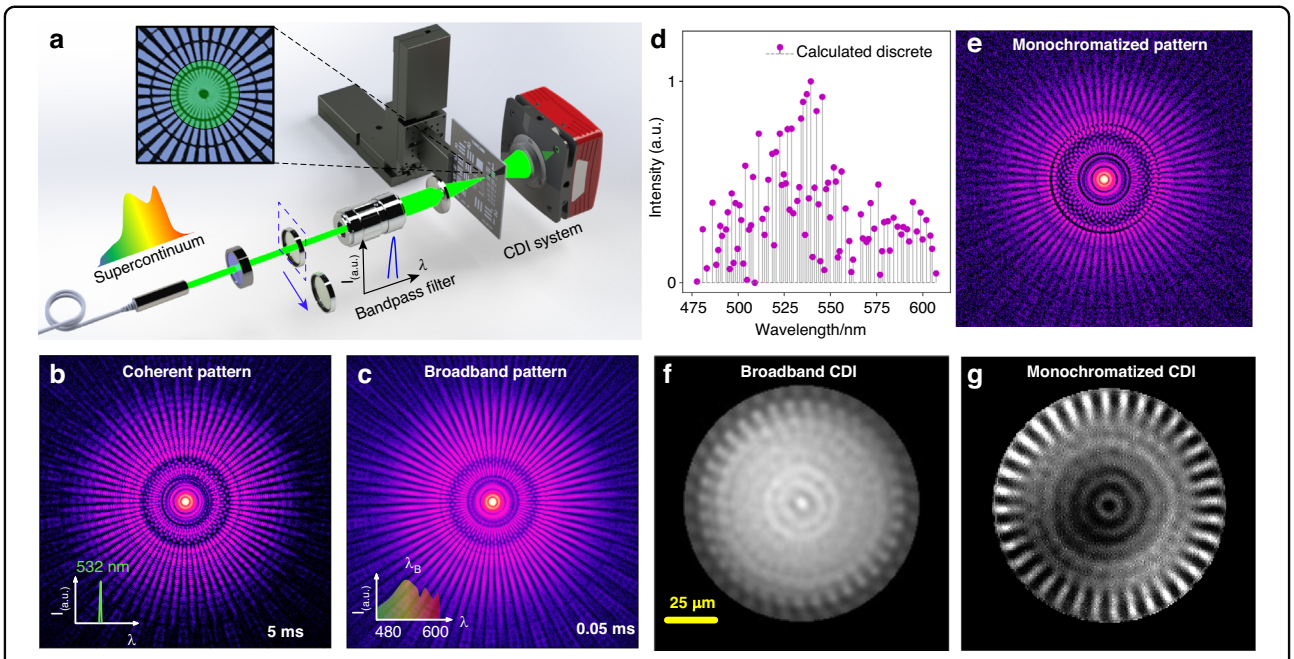

Fig. 5 A typical application of broadband CDI using the proposed diffraction-based computational spectrometer. a The schematic layout of the broadband CDI set-up. **b** The pre-captured coherent pattern at 532 nm with 5 ms exposure time. **c** The corresponding broadband pattern captured in situ with up to 20% bandwidth (spectrum ranging from 480 nm to 600 nm) with only 0.05 ms exposure time. **d** The aftermost calculated spectrum components of the system at the detector plane from the diffraction datasets given in (**b**, **c**). **e** The monochromatized pattern recovered from the broadband data in (**c**) applying the calculated spectrum components in (**d**). **f** CDI results from the broadband data in (**c**). **g** CDI results from the monochromatized data in (**e**). All diffraction patterns are log-scaled

pinhole, as shown in Fig. 4e. The refined design of the diffraction disperser boosts diffraction efficiency, consequently enhancing the quality of spectrum reconstruction. Meanwhile, the spectral response bandwidth of the spectrometer is predominantly limited by the detector QE.

Additionally, the resolution of peak separation of the bimodal spectrum may also degenerate from the decoherence of the pre-captured diffraction, which is used to generate the PSFs over the full spectrum range. The better the coherency of the quasi-monochromatic diffraction, the higher the resolution of spectral peak separation (details in Supplementary S5).

Discussion

A fancy application of broadband lensless imaging was further implemented to demonstrate the prospect of the proposed novel spectrometer in practical applications. Figure 5 shows the layout of a broadband CDI set-up (details in Supplementary S6) and the reconstructions by utilizing the developed approach compared with results based on conventional phase retrieval techniques. It should be mentioned that the strict requirement of narrowband radiation with high coherency in current CDI architectures poses a significant obstacle to achieving efficient photon utilization across the full spectrum[45]. Numerous studies have been conducted to overcome this trade-off for broadband CDI in recent years[39,40,46–50], but encounter several formidable challenges, including the stringent constraints for non-dispersive specimens over full spectrum, the need for accurate spectrum measurement as input, and the requirement for the solutions to converge within the band limit to be valid. These issues severely hamper the advancement in CDI for the ultra-wide spectrum. At the same time, the proposed approach can break through these limitations and enable high-quality CDI even using broadband (i.e., incoherent) illumination without the requirement of any *prior* spectra (e.g., broadband illumination, the spectral transfer function of the specimen, or detector QE).

The aftermost transmission spectrum of the system at the detector plane (Fig. 5d) can be successfully resolved from the pre-captured coherent quasi-monochromatic diffraction pattern (Fig. 5b) and the broadband diffraction pattern in-situ with a bandwidth of 20%, spanning from 480 nm to 600 nm (Fig. 5c) by the proposed method. Then, as demonstrated in Fig. 5e, the monochromatized diffraction pattern can be retrieved from the corresponding broadband diffraction utilizing a numerical monochromatization method[39] (details in Supplementary S7). Noting that the broadband pattern displayed a significant reduction in coherence compared

to the coherent pattern. This decrease in coherence ultimately resulted in a convergence failure during the CDI reconstruction process (Fig. 5f). However, the monochromatization by the proposed method effectively addresses this decoherence issue arising from the broadband radiation. Furthermore, a comparison of CDI results was eventually performed by 500 iterations of RAAR[51] from the broadband pattern and monochromatized pattern, respectively. Compared with the CDI result from the broadband pattern (Fig. 5f), the monochromatized CDI (Fig. 5g) showcases a remarkable improvement in the quality of the reconstruction with high fidelity. The good spectral agreement and high quality of the broadband CDI results demonstrate the superiority of the proposed approach, implying huge potential applications not only in broadband spectrum metrology with high resolution but also in fields of rising computational imaging techniques.

In summary, we have proposed a novel scheme of computational spectrometer based on the one-to-broadband diffraction applying a simplified and arbitrarily shaped diffraction microstructure as the disperser, which makes the device ultra-compact and low-cost and paves the way towards single-shot spectrum metrology. Different from other computational spectrometer designs, the proposed spectrometer is based on the PSF mapping from a single shot of pre-captured coherent monochromatic diffraction to generate a full spectral response function, and it does not require pre-encoding design, complex fabrication with high precision, or full spectral response function calibration. Experiments conducted on a proof-of-concept have verified the methodology, and results indicate that the proposed computational spectrometer provides a spectral resolution better than 3 nm and the accuracy of the spectral peak is better than 1 nm over a 200 nm bandwidth. Benefiting from its generality of principle, simple architecture, and compact size, the proposed approach has great potential in a huge range of applications in broadband spectrum metrology and computational imaging with miniaturized, cost-effective, and lab-on-chip integration. A broadband CDI prototype is successfully implemented based on the proposed approach to practically demonstrate a fancy application in broadband lensless imaging, which successfully tackles all the challenges of the current state-of-the-art broadband phase retrieval techniques (e.g., the ultra-broadband illumination with unknown spectrum, free of spectral correction of the specimen or detector QE). The proposed method can be easily extended and applied to optical techniques and systems related to multi-state coherent diffraction superposition, such as phase-retrieval-based computational imaging systems with broadband or multi-wavelength illumination.

Materials and methods

PSFs calculation

The bandwidth of the incident spectrum is uniformly divided into n slices λ_1, λ_2,..., λ_n, the PSF at an arbitrary wavelength λ_i distributes as a scale from a monochromatic diffraction pattern I_m at a wavelength λ_m:

$$PSF(\lambda_i, x_i, y_i) = \frac{c}{\lambda_i z}\begin{bmatrix} \lambda_i/\lambda_m & 0 & M(\lambda_m-\lambda_i)/\lambda_m \\ 0 & \lambda_i/\lambda_m & N(\lambda_m-\lambda_i)/\lambda_m \end{bmatrix}\begin{bmatrix} x_m \\ y_m \\ 1 \end{bmatrix} \tag{5}$$

where x_i, y_i denotes the coordinates of the diffraction pattern at a wavelength λ_i, and M, N is the total number of pixels in the captured diffraction pattern along the X, Y direction, respectively. Seeing that the $PSF(\lambda_i)$ is an affine transformation from a reference diffraction field $\sqrt{I_m}$ where λ_i/λ_m is the scaling factor to describe the PSF mapping and $(M(\lambda_m-\lambda_i)/\lambda_m,\ N(\lambda_m-\lambda_i)/\lambda_m)$ is the translation factor to center the scaled diffraction orders. It is worth noting that since each pixel's readout value represents the sum of diffraction intensities across all spectral channels, the PSF mapping matrix should be resampled by performing interpolation such that the spatial resolution of $PSF(\lambda_i)$ matches the sensor pixel size. Additionally, λ_m would be carefully selected around the mass of the center of the broadband spectrum to reduce the PSF mapping error from interpolation (details in Supplementary S8).

Spectrum reconstruction

A broadband diffraction I_B is the integral of $\omega(\lambda)[PSF(\lambda_i)]^2$ over the wavelength range, which can be performed as an MLR model by summing n discrete slices in spectra range for approximation, rewritten to a matrix form in simplicity:

$$I_B = \sum_{i=1}^{n} \omega(\lambda_i)[PSF(\lambda_i)]^2 \overset{\text{Simplicity}}{\Rightarrow} \boldsymbol{A\omega} = \boldsymbol{b} \tag{6}$$

Note that the formula of Eq. (6) is a system of $M \times N$ multi-linear simultaneous equations with n-dimensional parameter vector, where $\boldsymbol{A}$ is a given $M \times N \times n$ matrix with elements of each column of a flattened $PSF(\lambda_i)$ matrix in 1D array corresponding to the ith slice of spectrum and $\boldsymbol{b}$ is a known vector of a recorded broadband diffraction flattened in 1D array, $\boldsymbol{\omega}$ is the vector of unknown spectrum coefficients for the function. Practically, it is usually impossible to solve the MLR by ordinary noniterative methods due to its ill-posed nature. To tackle such instabilities, a method of residual norm minimization is applied with a weighting regularization factor, as known as Tikhonov regularization, to reconstruct the power spectrum $\boldsymbol{\omega}$ and

suppress the noise signals during reconstruction. The least square of the sum of squared residuals with a regularization item is minimized as

$$\hat{\boldsymbol{\omega}} = \underset{\omega}{argmin} \|\boldsymbol{A\omega} - \boldsymbol{b}\|_2^2 + \Gamma^2\|\boldsymbol{\omega}\|_2^2, \Gamma > 0 \quad (7)$$

where Γ is the regularization coefficient, $\|.\|_2$ is the l_2 norm. Note that the efficiency of these estimates depends on the appropriate choice of the regularization coefficient Γ, which should be carefully selected to balance the results of robustness and resolution. Here, we use the GCV statistic to select the regularization coefficient adaptively[52]. As a result, we can have the power spectrum estimates $\hat{\boldsymbol{\omega}}$ from Tikhonov regularization Eq. (7).

Since the total components in a measurement of power spectrum $\hat{\boldsymbol{\omega}}$ distributes sparsely, corresponding to its spectral sampling interval $\delta\lambda$ in Eq. (3), a linear fitting with a uniform interval is processed to resample the calculated dataset. Finally, the finer reconstruction of an incident spectrum is optimized by a convolution operator with a Hann window to suppress high-frequency interference. The workflow of the proposed computational diffraction-based microspectrometer is detailed in Supplementary S2.

Acknowledgements
The authors thank the technical support from the Experiment Centre for Advanced Manufacturing and Technology in the School of Mechanical Science &Engineering of HUST. This work was supported by the National Natural Science Foundation of China (52130504), Key Research and Development Program of Hubei Province (2021BAA013), Innovation Project of Optics Valley Laboratory (OVL2023PY003), Natural Science Foundation of Hubei Province (2021CFB322), Fundamental Research Funds for the Central Universities (2021XXJS113), and Guangdong Basic and Applied Basic Research Foundation (2023A1515030149).

Author contributions
C.C. conceived the project, conducted the experiments, performed the algorithm derivation, and analyzed the spectroscopic data. L.S. and G.H. conceived and supervised the project. C.C., L.S., and G.H. drafted the paper.

Data availability
The data and codes that support the plots within this paper and other findings of this study are available from the corresponding author upon reasonable request. Source data are provided in this paper.

Code availability
The data and codes that support the plots within this paper and other findings of this study are available from the corresponding author upon reasonable request. Source data are provided in this paper.

Conflict of interest
The authors declare no competing interests.

Supplementary information The online version contains supplementary material available at https://doi.org/10.1038/s41377-023-01355-4.

Received: 13 August 2023 Revised: 7 December 2023 Accepted: 8 December 2023
Published online: 05 January 2024

References

1. Wolffenbuttel, R. F. State-of-the-art in integrated optical microspectrometers. *IEEE Trans. Instrum. Meas.* **53**, 197–202 (2004).
2. Yang, Q. F. et al. Vernier spectrometer using counterpropagating soliton microcombs. *Science* **363**, 965–968 (2019).
3. Bacon, C. P., Mattley, Y. & DeFrece, R. Miniature spectroscopic instrumentation: applications to biology and chemistry. *Rev. Sci. Instrum.* **75**, 1–16 (2004).
4. Buchberger, A. R. et al. Mass spectrometry imaging: a review of emerging advancements and future insights. *Anal. Chem.* **90**, 240–265 (2018).
5. Debaes, C. et al. Deep proton writing: a rapid prototyping polymer microfabrication tool for micro-optical modules. *N. J. Phys.* **8**, 270 (2006).
6. Hansen, P. C. REGULARIZATION TOOLS: a matlab package for analysis and solution of discrete ill-posed problems. *Numer. Algorithms* **6**, 1–35 (1994).
7. Tikhonov, A. N. On the solution of ill-posed problems and the method of regularization. *Dokl. Akad. Nauk SSSR* **151**, 501–504 (1963).
8. Kwa, T. A. & Wolffenbuttel, R. F. Integrated grating/detector array fabricated in silicon using micromachining techniques. *Sens. Actuators A* **31**, 259–266 (1992).
9. He, J. J. et al. Monolithic integrated wavelength demultiplexer based on a waveguide Rowland circle grating in InGaAsP/InP. *J. Lightwave Technol.* **16**, 631–638 (1998).
10. Sander, D. & Müller, J. Selffocussing phase transmission grating for an integrated optical microspectrometer. *Sens. Actuators A: Phys.* **88**, 1–9 (2001).
11. Huang, E., Ma, Q. & Liu, Z. W. Etalon array reconstructive spectrometry. *Sci. Rep.* **7**, 40693 (2017).
12. Faraji-Dana, M. S. et al. Compact folded metasurface spectrometer. *Nat. Commun.* **9**, 4196 (2018).
13. Zhu, A. Y. et al. Ultra-compact visible chiral spectrometer with meta-lenses. *APL Photonics* **2**, 036103 (2017).
14. Tittl, A. et al. Imaging-based molecular barcoding with pixelated dielectric metasurfaces. *Science* **360**, 1105–1109 (2018).
15. Wang, R. X. et al. Compact multi-foci metalens spectrometer. *Light* **12**, 103 (2023).
16. Goldman, D. S., White, P. L. & Anheier, N. C. Miniaturized spectrometer employing planar waveguides and grating couplers for chemical analysis. *Appl. Opt.* **29**, 4583–4589 (1990).
17. Cheben, P. et al. A high-resolution silicon-on-insulator arrayed waveguide grating microspectrometer with sub-micrometer aperture waveguides. *Opt. Express* **15**, 2299–2306 (2007).
18. Shi, Z. M. & Boyd, R. W. Fundamental limits to slow-light arrayed-waveguide-grating spectrometers. *Opt. Express* **21**, 7793–7798 (2013).
19. Babin, S. et al. Digital optical spectrometer-on-chip. *Appl. Phys. Lett.* **95**, 041105 (2009).
20. Calafiore, G. et al. Holographic planar lightwave circuit for on-chip spectroscopy. *Light* **3**, e203 (2014).
21. Gao, B. S., Shi, Z. M. & Boyd, R. W. Design of flat-band superprism structures for on-chip spectroscopy. *Opt. Express* **23**, 6491–6496 (2015).
22. Momeni, B., Hosseini, E. S. & Adibi, A. Planar photonic crystal microspectrometers in silicon-nitride for the visible range. *Opt. Express* **17**, 17060–17069 (2009).
23. Correia, J. H. et al. Single-chip CMOS optical microspectrometer. *Sens. Actuators A* **82**, 191–197 (2000).
24. Wang, S. W. et al. Concept of a high-resolution miniature spectrometer using an integrated filter array. *Opt. Lett.* **32**, 632–634 (2007).
25. Pervez, N. K. et al. Photonic crystal spectrometer. *Opt. Express* **18**, 8277–8285 (2010).
26. Emadi, A. et al. Design and implementation of a sub-nm resolution microspectrometer based on a Linear-Variable Optical Filter. *Opt. Express* **20**, 489–507 (2012).
27. DeCorby, R. G. et al. Chip-scale spectrometry based on tapered hollow Bragg waveguides. *Opt. Express* **17**, 16632–16645 (2009).
28. Cen, Q. Q. et al. Microtaper leaky-mode spectrometer with picometer resolution. *eLight* **3**, 9 (2023).
29. Liapis, A. C. et al. On-chip spectroscopy with thermally tuned high-Q photonic crystal cavities. *Appl. Phys. Lett.* **108**, 021105 (2016).
30. Little, B. E. et al. Ultra-compact Si-SiO_2 microring resonator optical channel dropping filters. *IEEE Photonics Technol. Lett.* **10**, 549–551 (1998).
31. Nitkowski, A., Chen, L. & Lipson, M. Cavity-enhanced on-chip absorption spectroscopy using microring resonators. *Opt. Express* **16**, 11930–11936 (2008).

32. Xu, H. N. et al. Breaking the resolution-bandwidth limit of chip-scale spectrometry by harnessing a dispersion-engineered photonic molecule. *Light* **12**, 64 (2023).
33. Bao, J. & Bawendi, M. G. A colloidal quantum dot spectrometer. *Nature* **523**, 67–70 (2015).
34. Zhu, X. X. et al. Broadband perovskite quantum dot spectrometer beyond human visual resolution. *Light* **9**, 73 (2020).
35. Yang, Z. Y. et al. Single-nanowire spectrometers. *Science* **365**, 1017–1020 (2019).
36. Redding, B. et al. Evanescently coupled multimode spiral spectrometer. *Optica* **3**, 956–962 (2016).
37. Redding, B. et al. Compact spectrometer based on a disordered photonic chip. *Nat. Photonics* **7**, 746–751 (2013).
38. Xu, Z. C. et al. Multimodal multiplex spectroscopy using photonic crystals. *Opt. Express* **11**, 2126–2133 (2003).
39. Huijts, J. et al. Broadband coherent diffractive imaging. *Nat. Photonics* **14**, 618–622 (2020).
40. Witte, S. et al. Lensless diffractive imaging with ultra-broadband table-top sources: from infrared to extreme-ultraviolet wavelengths. *Light* **3**, e163 (2014).
41. Wang, P. & Menon, R. Computational spectrometer based on a broadband diffractive optic. *Opt. Express* **22**, 14575–14587 (2014).
42. Yang, T. et al. Miniature spectrometer based on diffraction in a dispersive hole array. *Opt. Lett.* **40**, 3217–3220 (2015).
43. Paganin, D. *Coherent X-Ray Optics*. (Oxford University Press, Oxford, 2006).
44. Golub, G. H., Heath, M. & Wahba, G. Generalized cross-validation as a method for choosing a good ridge parameter. *Technometrics* **21**, 215–223 (1979).
45. Whitehead, L. W. et al. Diffractive imaging using partially coherent X rays. *Phys. Rev. Lett.* **103**, 243902 (2009).
46. Liu, R. F. et al. Broadband ptychographic imaging with an accurately sampled spectrum. *Phys. Rev. A* **107**, 033510 (2023).
47. Goldberger, D. et al. Single-pulse, reference-free, spatiospectral measurement of ultrashort pulse-beams. *Optica* **9**, 894–902 (2022).
48. Li, W. et al. Lensless imaging through thin scattering layers under broadband illumination. *Photonics Res.* **10**, 2471–2487 (2022).
49. Johnson, A. S. et al. Quantitative hyperspectral coherent diffractive imaging spectroscopy of a solid-state phase transition in vanadium dioxide. *Sci. Adv.* **7**, eabf1386 (2021).
50. Abbey, B. et al. Lensless imaging using broadband X-ray sources. *Nat. Photonics* **5**, 420–424 (2011).
51. Luke, D. R. Relaxed averaged alternating reflections for diffraction imaging. *Inverse Probl.* **21**, 37–50 (2005).
52. Mitrouli, M. & Roupa, P. Estimates for the generalized cross-validation function via an extrapolation and statistical approach. *Calcolo* **55**, 24 (2018).
53. Pohl, D. et al. An integrated broadband spectrometer on thin-film lithium niobate. *Nat. Photonics* **14**, 24–29 (2020).
54. Zhang, W. Y. et al. Deeply learned broadband encoding stochastic hyperspectral imaging. *Light* **10**, 108 (2021).
55. Fröch, J. E. et al. Dual band computational infrared spectroscopy via large aperture meta-optics. *ACS Photonics* **10**, 986–992, (2023).

Supplementary Information for

Ultra-simplified diffraction-based computational spectrometer

Chuangchuang Chen[a], Honggang Gu[a,b,*], Shiyuan Liu[a,b,*]

[a] *State Key Laboratory of Intelligent Manufacturing Equipment and Technology, Huazhong University of Science and Technology, Wuhan, Hubei 430074, China*

[b] *Optics Valley Laboratory, Wuhan, Hubei 430074, China*

[*] *Corresponding authors: hongganggu@hust.edu.cn (H. Gu); shyliu@hust.edu.cn (S. Liu)*

S1 Broadband Fraunhofer diffraction approximation from PSF superposition

Consider a monochromatic plane wave with a wavelength λ propagated from a hollow microstructure (constant transmission over full spectrum) couples the amplitude and phase of a diffraction field $\psi_\lambda(x,y,z)$ by traveling a distance of z, in the paraxial approximation, given by the Fraunhofer diffraction formula[1]:

$$\psi_\lambda(x,y,z)=\frac{e^{i2\pi z/\lambda}}{i\lambda z}\mathrm{e}^{i\pi\left(x^2+y^2\right)/\lambda z}\,\mathrm{F}\,\left\{U(x',y',0)\right\}\Big|_{u=\frac{x}{\lambda z},v=\frac{y}{\lambda z}} \tag{S1}$$

where $\mathcal{F}$ denotes the 2D spatial Fourier transform of the exit wave function $U(x',y',0)$ at z = 0, with u and v the spatial frequencies. In case of broadband radiation, the broadband diffracted field Φ can be written as:

$$\Phi(\lambda)=\sqrt{\omega(\lambda)}\psi_\lambda(x,y,z) \tag{S2}$$

where $\omega(\lambda)$ is the power spectrum density of the incident radiation. The broadband diffraction field in spatial domain can be obtained by an inverse Fourier transform:

$$\Phi(t)=\frac{1}{\sqrt{2\pi}}\int\Phi(\lambda)e^{i\lambda t}d\lambda \tag{S3}$$

Since only the amplitude of diffraction is recorded by the detector, while the phase information is dropped, the detector integrates over time to produce the broadband diffraction pattern I_B:

$$I_B=\int\left|\Phi(t)\right|^2dt=\frac{1}{2\pi}\int\left|\Phi(\lambda)\right|^2d\lambda \tag{S4}$$

with using Parseval's theorem. By Eq. (S2) substituted into Eq. (S4), we have I_B:

$$I_B=\frac{1}{2\pi}\int\omega(\lambda)\left|\psi_\lambda\right|^2d\lambda \tag{S5}$$

Known that a recorded monochromatic diffraction pattern I_λ can be written as:

$$I_\lambda=\left|\psi_\lambda\right|^2=\left(\frac{c}{\lambda z}\left|\mathrm{F}\,\left\{U(x',y',0)\right\}\right|_{u=\frac{x}{\lambda z},v=\frac{y}{\lambda z}}\right)^2 \tag{S6}$$

Seeing that Fraunhofer diffraction intensity distribution depends only on the propagation distance z and wavelength λ in an identical way, showing a wavelength-dependent factor $c/\lambda z$, which allows us to map a coherent diffraction I_λ at an arbitrary wavelength from a single coherent diffraction shot I_m at a given wavelength λ_m by PSF propagation between different spectral components. Introducing the scaling factor λ_i/λ_m, the PSF mapping can be described as:

$$PSF\left(\lambda_i, x_i, y_i\right) = \frac{c}{\lambda_i z}\begin{vmatrix} \frac{\lambda_i}{\lambda_m} & 0 & M\frac{\lambda_m - \lambda_i}{\lambda_m} \\ 0 & \frac{\lambda_i}{\lambda_m} & N\frac{\lambda_m - \lambda_i}{\lambda_m} \end{vmatrix}\begin{vmatrix} x_m \\ y_m \\ 1 \end{vmatrix} \tag{S7}$$

where x_i, y_i denotes the coordinates of the diffraction field $|\psi_i|$ at a wavelength λ_i, and M, N is the total number of pixels in the captured diffraction pattern. Seeing that the $PSF(\lambda_i)$ is an affine transformation from a reference diffraction filed $\sqrt{I_m}$ where λ_i/λ_m is the scaling factor to describe the PSF mapping and ($M(\lambda_m - \lambda_i)/\lambda_m$, $N(\lambda_m - \lambda_i)/\lambda_m$) is the translation factor to center the scaled diffraction orders.

Thus, combined with Eq. (S5~S7), the broadband diffraction pattern I_B can be approximately rewritten as an integration of PSFs from the reference diffraction filed $\sqrt{I_m}$, weighted by the power spectrum $\omega(\lambda)$ over full spectral bandwidth of radiation:

$$I_B = \int \omega(\lambda)\left[PSF(\lambda)\right]^2 d\lambda\,. \tag{S8}$$

S2 Spectrum measurement workflow from a single-shot broadband diffraction

Input:

✧ I_m: Pre-captured quasi-monochromatic diffraction pattern at a wavelength λ_m (Fig. S1a).

✧ QE(λ): Detector's absolute QE (Fig. S1d).

Step 1: Single-shot broadband diffraction measurement

Capture a single-shot broadband diffraction pattern I_B at an unknown wide spectrum, as shown in Fig. S1**b**. Noting that the zero-order diffractions are overexposed and the background noise of detector is removed to better utilize the detector sensor's dynamic range[2], the central fringe saturation is consequently filtered from the detector before data processing, as demonstrated in Fig. S1 **a, b**.

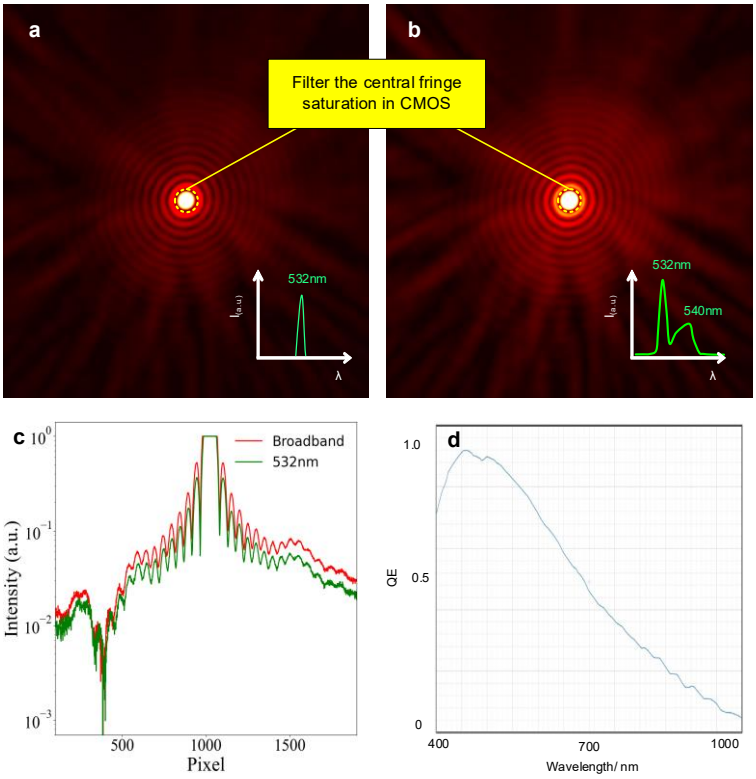

Figure S1 Inputs for the spectrum measurement. a, the pre-captured quasi-monochromatic diffraction pattern I_m at 532 nm with 3 nm FWHM. **b**, the Measured broadband diffraction from unknown spectrum radiation. **c** plots vertical line cuts along the center of the diffraction patterns in **a** and **b**, respectively. **d**, the absolute QE of the detector with spectral response >0.2 ranging from 400nm to 800nm

Step 2: Calculate PSFs

Give an initial prediction of the spectrum range, where the bandwidth is usually large than the ground truth. Then, the spectrum is divided uniformly into *n* slices $\lambda_1, \lambda_2, \ldots \lambda_n$ by the interval $\delta\lambda$ uniformly. Practically, $\delta\lambda$ is limited by the detector pixel size d_p, the recorded diffraction length D with high SNR, and the referenced wavelength λ_m, given by:

$$\delta\lambda = \frac{\lambda_m d_p}{D} \tag{S9}$$

Then, a series of PSFs is calculated from the pre-captured I_m by Eq. (S7). Figure S2 plots the distribution of n slices of calculated PSFs in 1D case over ranges of spectrum components. It is worth noting that the PSF mapping matrix should be resampled by performing interpolation such that the spatial resolution of $PSF(\lambda_i)$ matches the sensor pixel size. In this work, a linear interpolation[3] is performed to resample the PSFs with the interval steps the same as the pixel size of the detector.

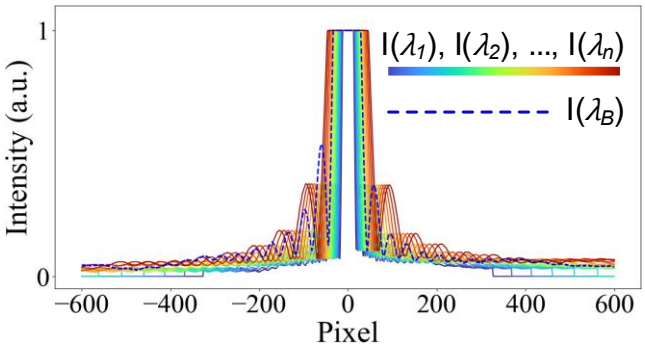

Figure S2 Distribution of PSFs in 1D-case by scanning the wavelength over ranges of spectrum components.

Step 3 Solving spectrum via MLR scheme

Due to the measurement noise in both I_B and I_m combined with the approximation errors in PSF mapping which make the Eq. (S8) ill-posed, it is generally impossible to solve these equations straightforwardly by ordinary noniterative methods. Note that the formula of Eq. (S8) is a system of $\mathrm{M} \times \mathrm{N}$ multi-linear simultaneous equations with n-dimensional parameter vector. We rewrite Eq. (S8) to a matrix form in simplicity as:

$$\boldsymbol{A\omega} = \boldsymbol{b} \tag{S10}$$

where

$$\boldsymbol{b} = \left[I_B(x_1, y_1) \quad I_B(x_1, y_2) \quad \cdots \quad I_B(x_1, y_N) \quad \cdots I_B(x_M, y_N) \right]^T$$

$$\boldsymbol{A} = \begin{bmatrix} \left[PSF(x_1, y_1, \lambda_1)\right]^2 & \left[PSF(x_1, y_1, \lambda_2)\right]^2 & \cdots & \left[PSF(x_1, y_1, \lambda_n)\right]^2 \\ \left[PSF(x_1, y_2, \lambda_1)\right]^2 & \left[PSF(x_1, y_2, \lambda_2)\right]^2 & \cdots & \left[PSF(x_1, y_2, \lambda_n)\right]^2 \\ \vdots & \vdots & \ddots & \vdots \\ \left[PSF(x_1, y_N, \lambda_1)\right]^2 & \left[PSF(x_1, y_N, \lambda_2)\right]^2 & \cdots & \left[PSF(x_1, y_N, \lambda_n)\right]^2 \\ \vdots & \vdots & \ddots & \vdots \\ \left[PSF(x_M, y_N, \lambda_1)\right]^2 & \left[PSF(x_M, y_N, \lambda_2)\right]^2 & \cdots & \left[PSF(x_M, y_N, \lambda_n)\right]^2 \end{bmatrix}$$

$$\boldsymbol{\omega} = \left[\omega(\lambda_1) \quad \omega(\lambda_2) \quad \cdots \quad \omega(\lambda_n)\right]^T$$

Note that Eq. (S10) is a form of MLR scheme, which is often fitted by minimizing a penalized version of the least squares cost function, as known as Tikhonov regularization[4], to reconstruct the power spectrum $\boldsymbol{\omega}$ and suppress the noise signals during reconstruction, given by

$$\hat{\boldsymbol{\omega}} = \underset{\omega}{\operatorname{argmin}} \left\|\boldsymbol{A}\boldsymbol{\omega} - \boldsymbol{b}\right\|_2^2 + \Gamma^2 \left\|\boldsymbol{\omega}\right\|_2^2, \ \Gamma > 0 \tag{S11}$$

where Γ is the regularization coefficient, $\|.\|_2$ is the l_2 norm. Since the efficiency of these estimates depends on an appropriate choice of the regularization coefficient Γ, which should be carefully selected to balance the results of robustness and resolution. In this work, we employ a GCV (Generalized Cross-Validation) statistic to make the balanced choice of Γ adaptively[5]:

$$\hat{\Gamma} = \underset{\Gamma}{\operatorname{argmin}} \frac{\left\|\boldsymbol{A}\hat{\boldsymbol{\omega}} - \boldsymbol{b}\right\|_2^2}{\left[n - Tr\left(\boldsymbol{A}\left(\boldsymbol{A}^T\boldsymbol{A} + \Gamma^2 I\right)^{-1}\boldsymbol{A}^T\right)\right]^2} \tag{S12}$$

where I is the identity matrix and the operator Tr sums elements on the main diagonal of a matrix. As a result, we can have the power spectrum estimates $\hat{\boldsymbol{\omega}}$ from solving Eq. (S11)

$$\hat{\boldsymbol{\omega}} = \left(\boldsymbol{A}^T\boldsymbol{A} + \Gamma^T\Gamma\right)^{-1}\boldsymbol{A}^T\boldsymbol{b} \tag{S13}$$

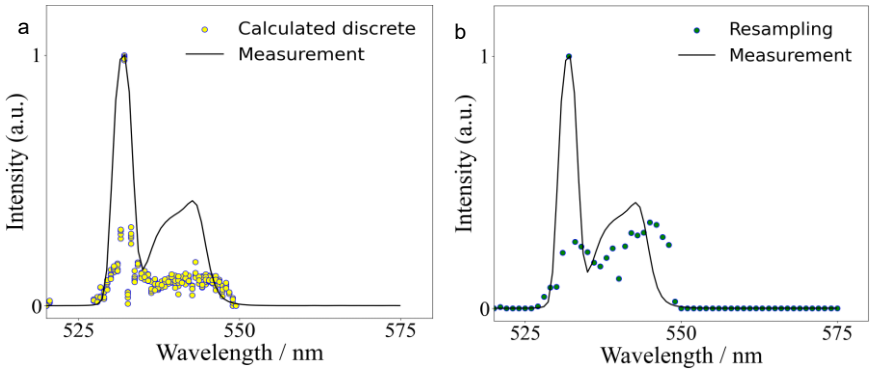

Figure S3 a, the distribution of PSFs in 1D-case by scanning the wavelength over ranges of spectrum components. **b**, the resampled results from **a** with a uniform interval $\Delta\lambda$

Note that the final power spectrum is obtained by distorting the detector's QE $\omega(\lambda) = \hat{\boldsymbol{\omega}}/\,QE(\lambda)$. Fig. S3**a** plots the calculated discrete power spectrum solutions. Since these scatters distribute irregularly along the wavelength axis, we resample the results with a uniform interval $\Delta\lambda$, which is several times of initial interval $\delta\lambda$ in Eq. (S9), as seen in Fig. S3**b**.

Step 4 Optimization via convolution process

We perform a convolution operator to the reconstructed data from step 3 with a Hann window to suppress high-frequency interference and reduce the effects of spectral leakage.

$$S(\lambda) = \hat{\omega}(\lambda) * h(\lambda) \tag{S14}$$

where * denotes convolution operator, $h(\lambda)$ is a Hann kernel with a size of N as:

$$h(\lambda) = \frac{1}{2}\left(1 - \cos\left(\frac{2\pi\lambda}{N-1}\right)\right) \tag{S15}$$

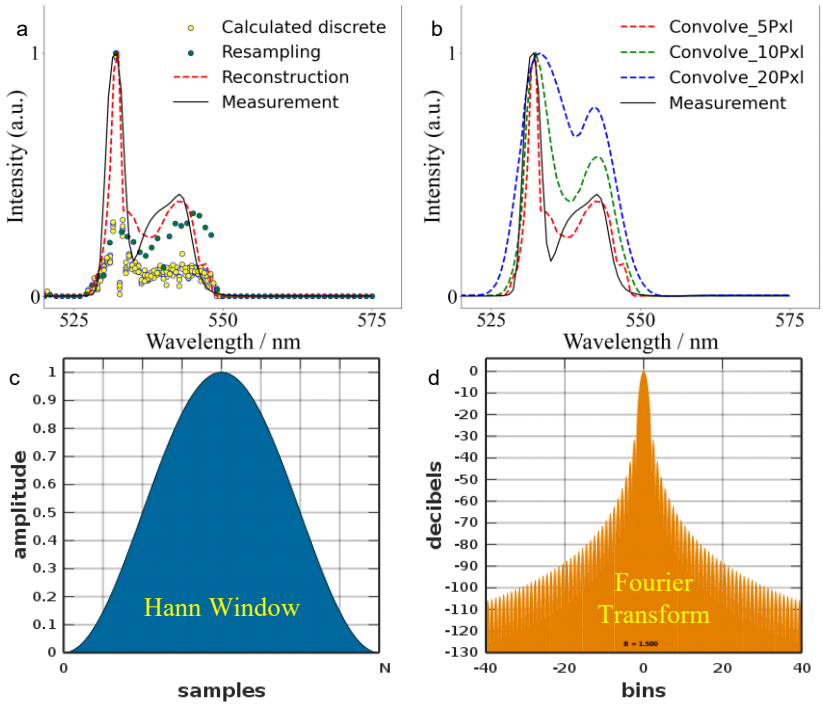

Figure S4 a, optimized result (red) which is convolved from the calculated resampled dataset (blue dots) with a Hann widow. **b,** a comparison of optimized results with different sizes of Hann kernels in the convolution process. The shape of Hann window and the corresponding Fourier transform is plotted in **c** and **d**, respectively.

Fig. S4**a** plots the results from a Hann windowing procedure. Seeing that the power spectrum profiles are accurately reconstructed and match well with the measurement. The high-frequency fluctuation is perfectly suppressed compared with the resampling data. However, it should be noticed that the windowing operator introduces somehow a decrease in resolution, which is very sensitive to the kernel size, where resolution of the reconstructions decreases when the kernel size increases (Fig. S4**b**). Thus, in practical applications, the kernel size should be carefully selected to balance the results of robustness and resolution.

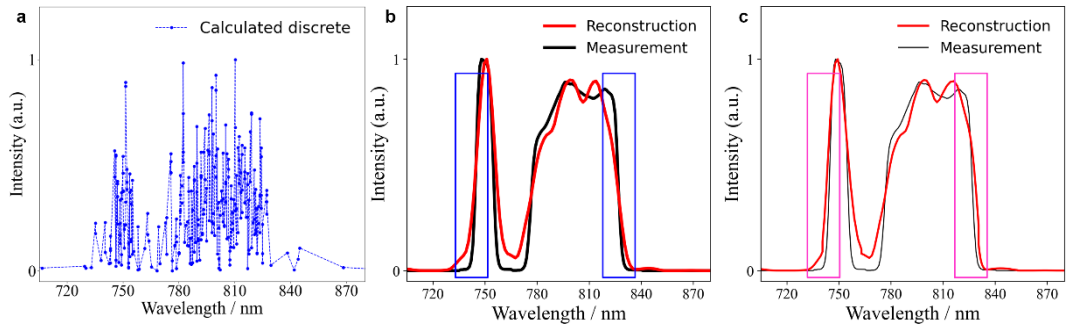

Figure S5 a, the calculated discrete spectrum components by the proposed diffraction-based computational spectrometer. **b**, the reconstructed spectrum mismatches with the measurement at the truncation points (blue boxes). **c**, the effect of mismatch is reduced by applying an intensive interpolation operator at the truncation points (pink boxes).

Additionally, the windowing operator may lead to matching errors in cases of transient signal, step signal, impulse response, or pulse signal applications. Fig. 5**a** gives an example of a truncated broadband spectrum reconstruction, seeing that there are mismatches at the truncation points (blue boxes). To tackle such mismatching, an intensive interpolation operator is applied to the truncation points to reduce the effects of match errors from convolution (pink boxes in Fig. S5**b**).

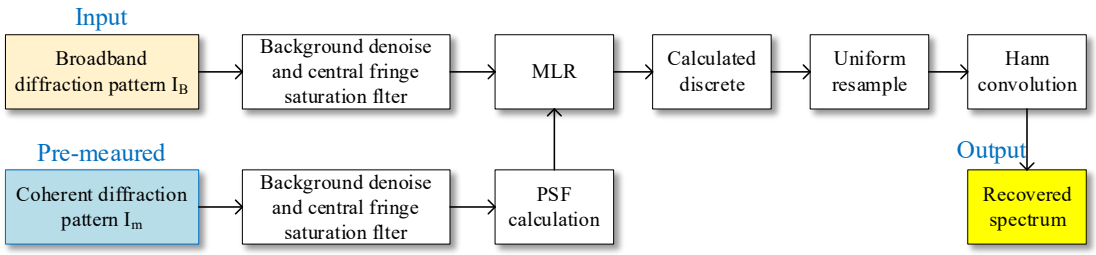

Figure S6 Spectrum measurement workflow from a single-shot broadband diffraction.

S3 Experimental set-up of the diffraction-based computational spectrometer

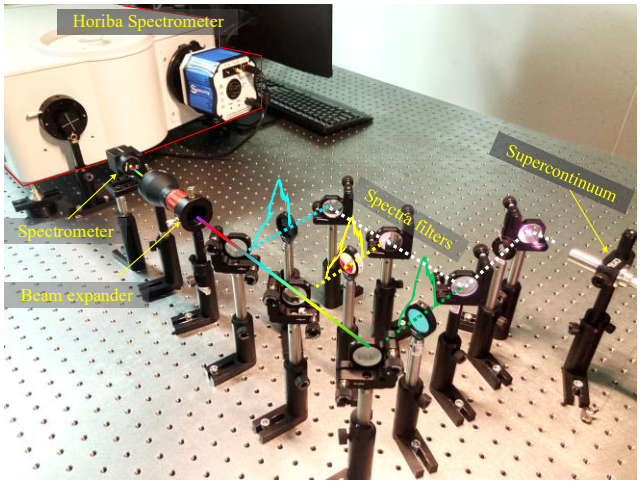

Figure S7 Experimental set up for the spectra measurements. A supercontinuum (YSL Photonics SC-Pro-M) is used to generate an ultra-broadband spectrum from 450nm to 1100nm. A set of optical filters (Thorlabs F series) is applied to the optical path to modulate the shape of incident spectra to different spectra profiles s as mentioned in the main test. The in-lab spectrometer is very compact in size to a $\emptyset 1"$ lens. All the spectra are pre-measured by a Horiba iHR 550 spectrometer as the measurements in ground truth.

S4 Nonlinearities of detector in the diffraction-based computational spectrometer

The proposed computational spectrometer relies on the coherent mode decomposition of broadband incoherent diffraction intensity. Since the diffraction intensity distribution exhibit an inherent characteristics of exceptionally bright central region alongside significantly dark high-order areas. This imposes critical demands on the detector for achieving high SNR during diffraction signal readout. It primarily involves three key aspects:

a) The dynamic range and spectral quantum efficiency of the detector sensor.

b) The suppression of detector noise in diffraction recording process.

c) Sensor size truncation on the active detector pixel array.

Dynamic range. In the context of Fraunhofer diffraction, most of the photon energy is concentrated within the central diffraction orders, while the higher-order diffracted photons are notably weaker. However, most of the redundant spectral dispersion information is mostly concentrated in the higher-order diffraction where the diffracted photons are dim. Hence, the commonly used detectors with 8-bit, 12-bit, or 16-bit analog-to-digital converter (ADC) dynamic ranges all prove inadequate in capturing the high-order diffraction signals without overexposure, as the simulations demonstrated in Fig. S8 a1~c1. To better use the detector sensor's dynamic range, we employ a specialized filter to eliminate central fringe saturations on the detector. This leads to a significant enhanced SNR for capturing high-order diffractions, as a comparison shown in Fig. S8 a2~c2.

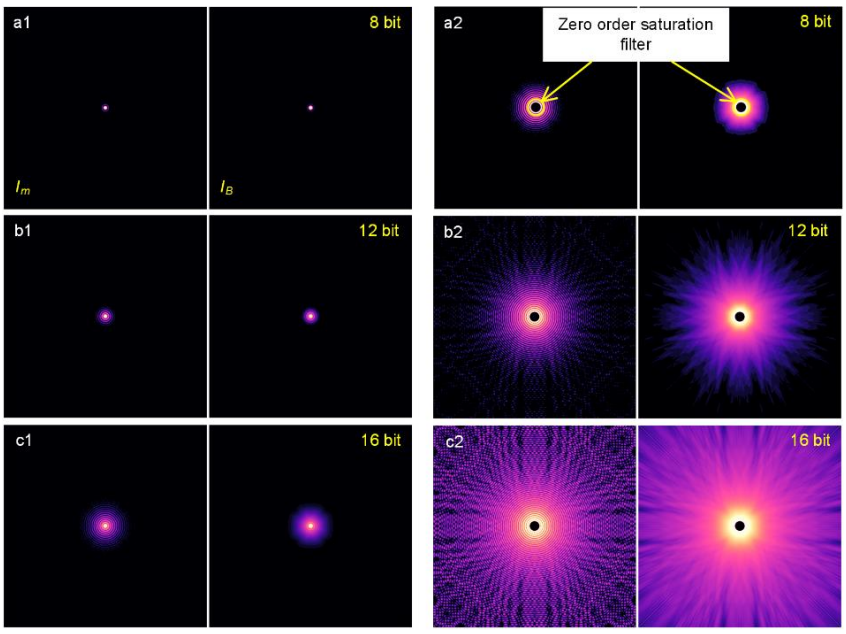

Figure S8 Simulation of the detector sensor dynamic range for diffraction recording. Rows a ~ c shows the captured monochromatic diffraction (left) and broadband diffraction (right) from the detector with varying dynamic ranges of 8 bits, 12 bits, and 16 bits, respectively. Column a1~c1 displays the under sampled diffraction data with no central stop, as a comparison in column a2~c2, a specialized filter is employed to eliminate the first several orders of overexposed diffractions.

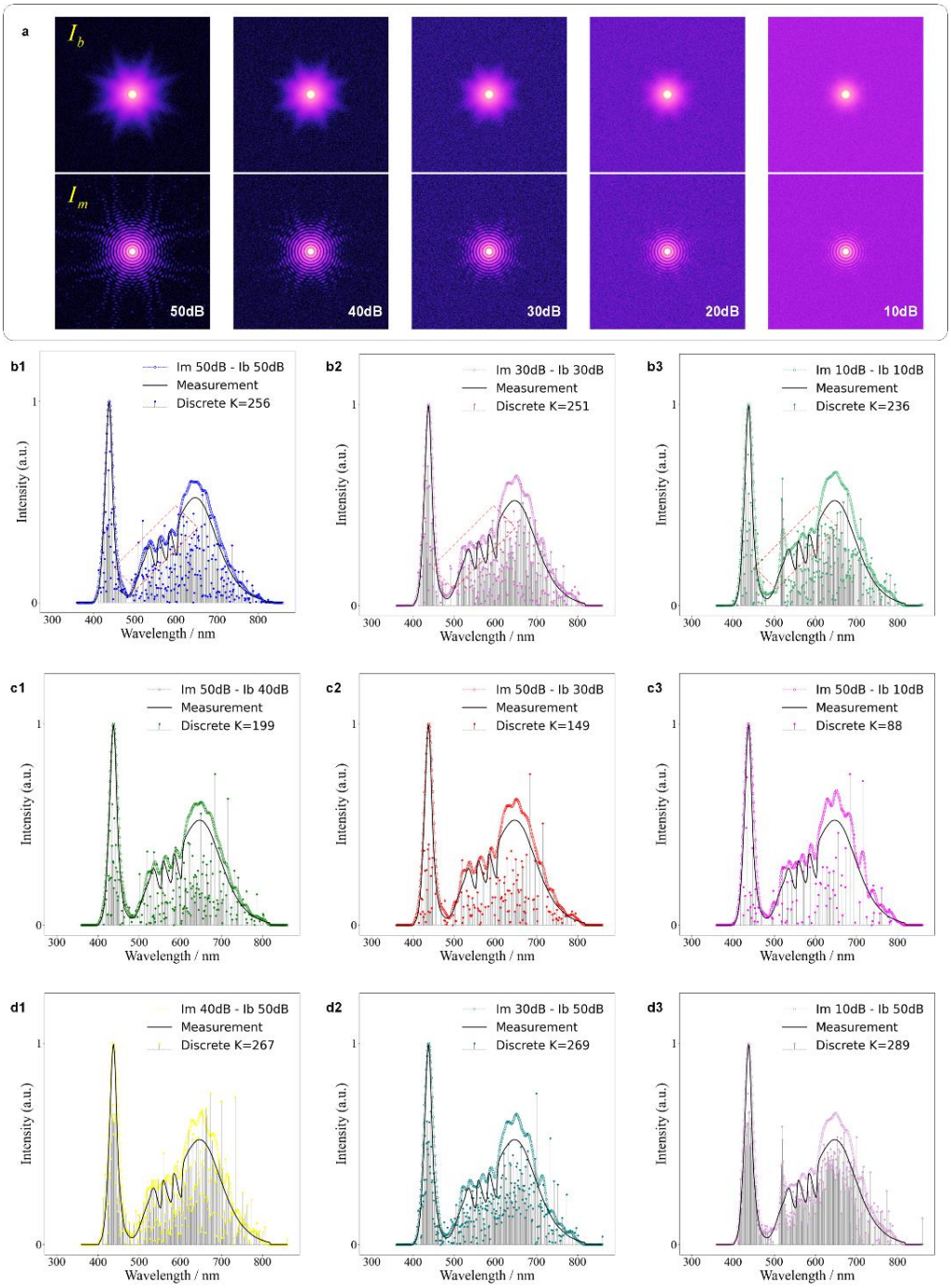

Figure S9 Simulation for varying levels of diffraction noises in spectrum measurement. a. varying levels of diffraction noises ranging from 50dB to 10dB (log scaled). Top row shows the corresponding broadband diffractions. Bottom row shows the monochromatic diffractions. Rows **b**~**d** plot the typical recovered spectra form the varying levels of noised diffractions in **a**, respectively. Row **b** shows the recovered spectra from the varying levels of noise in the pre-captured monochromatic diffraction and broadband diffraction ranging from 50dB to 10dB, respectively. Row **c** shows the recovered spectra from the varying levels of noise in the broadband diffraction ranging from 50dB to 10dB, respectively, while the pre-captured monochromatic diffraction is constant with 50dB noise. Row **d** shows the recovered spectra from the varying levels of noise in the pre-captured monochromatic diffraction ranging from 50dB to 10dB, respectively, while the broadband diffraction is constant with 50dB noise.

Detector noise. The presence of detector noise decreases the SNR in diffraction signal recording and therefore weakens the spectrum measurement accuracy. To this end, we utilized a widely-used noise model in HDR photography to analyze the primary noise sources in the acquisition of diffraction images[6,7]. The noise model includes several critical factors of camera noise, such as input scene radiant flux Φ, dark current D, sensor QE α, exposure time t, readout analog voltage (with saturation), analog amplifier g, and ADC, which can be simply modeled as a mixture of Gaussian noise and Poisson noise.

$$I \sim Poisson(t \cdot \alpha \cdot \Phi) \cdot g + Poisson(t \cdot g \cdot D) + Normal(0, \sqrt{\sigma_{read}^2 \cdot g^2 + \sigma_{ADC}^2}) \tag{S16}$$

Thus, the SNR in the detector can be qualified as the following formula:

$$\mathrm{SNR} = \frac{t \cdot \alpha \cdot \Phi}{\sqrt{t \cdot \alpha \cdot \Phi + t \cdot g \cdot D + R^2}} \tag{S17}$$

where R denotes the readout noise, which follows a Gaussian distribution. It's worth noting that the readout photon signal is constrained by the ADC dynamic range of the detector sensor.

Herein, we simulated detector noise in the proposed spectrometer by incorporating a combination of Gaussian and Poisson noise to the recording diffractions, with SNRs ranging from 50dB to 10dB, respectively, as demonstrated in Fig. S9 **a**. And the corresponding recovered spectra is plotted in Fig. S9 row **b**. Seeing that the proposed diffraction-based computational spectrometer reveals high robustness to noise. We observe that the reconstructed spectrum remains consistent with the ground truth, even under conditions of heavy noise, only tiny mismatches occur on steep turning points of the spectra, as indicated with the red dashed box in Fig. S9 row **b**.

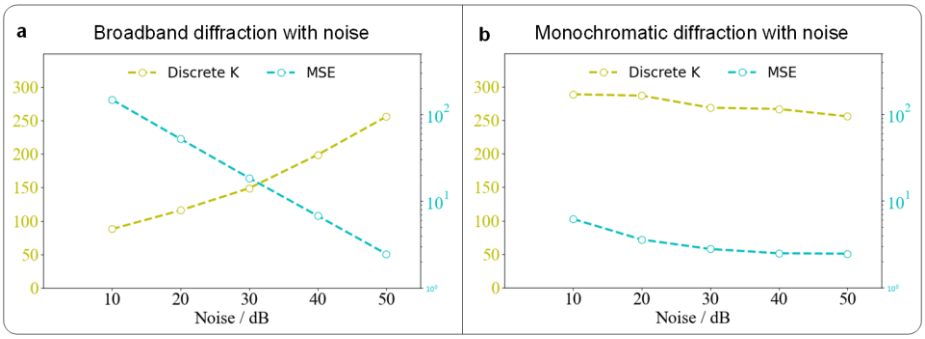

Figure S10 Number of the calculated spectra discrete and the prediction MSE corresponding to the measurements in broadband diffraction with varying noises in **a** and monochromatic diffraction with varying noises in **b**, respectively.

Additionally, we carried out a more extensive analysis to evaluate the noise robustness in the context of recording broadband diffractions and monochromatic diffractions. Fig. S9 rows **c**, **d** presents the comparison of recovered spectra under different levels of monochromatic and broadband diffraction noises. Meanwhile, we have monitored the

number of solved discrete power spectrum counts and the MSE in prediction during the spectrum calculation, as shown in Fig. S10. Seeing that the number of solved power spectrum counts increases with the noise power in broadband diffraction, whereas the MSE decreases simultaneously. In comparison, the computational spectrometer shows consistent robustness against varying noise power to the pre-captured monochromatic diffraction image. It is evident that the quality of spectrum measurement is more susceptible to noise in the presence of broadband diffraction images. This sensitivity arises from the spectrum's expansion, which results in diffraction aliasing, significantly reducing the coherence of the broadband diffraction signal and making it more vulnerable to noise. To this end, we practically employ a commonly used background noise minimization approach to suppress the detector noise in the diffraction image recording process[8].

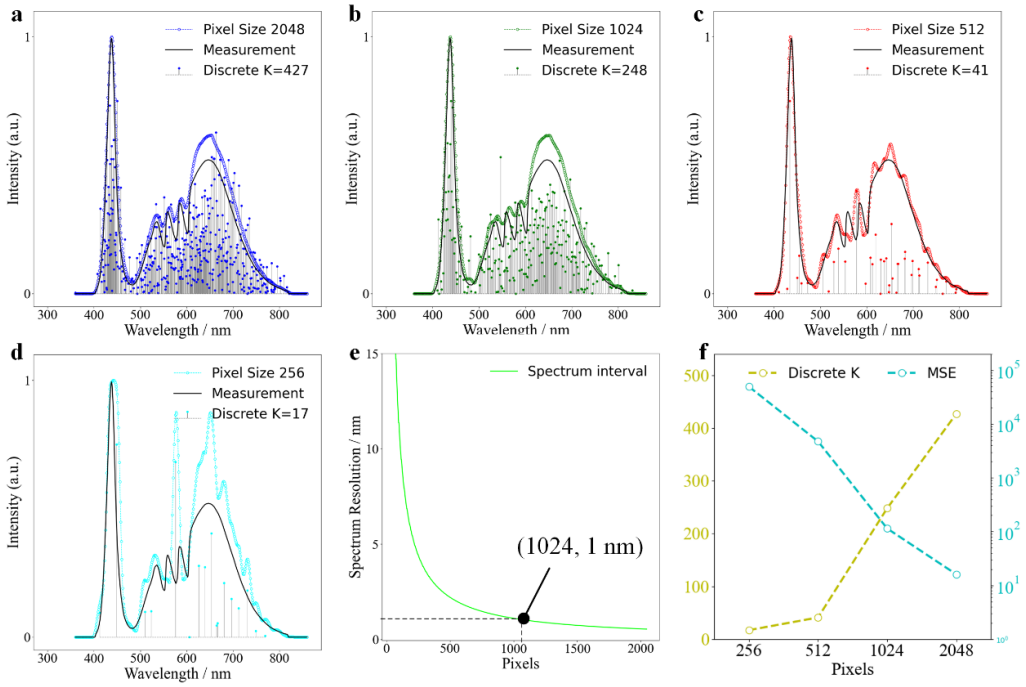

Figure S11 Truncation effect of the diffraction pattern by the finite detector array size in spectrum measurement. a~d showcase varying array size truncations by the finite detector in spectrum measurement. **e** plots the relationship of spectral measurement resolution with the number of sampling pixels. **f** shows the total number of the calculated spectra discrete and the prediction MSE corresponding to the measurements in broadband diffraction with varying sensor size truncations.

Sensor size truncation. As described in Eq. (3) in the main text, the spectral resolution of the proposed spectrometer ideally shows a reciprocal relationship with the number of sampling pixels in the active detector sensor array, primarily determined by the detector's dynamic range. In our pursuit of understanding the truncation effect caused by the finite detector array size in our spectrometer, a series of simulated analyses has been meticulously executed. As clearly depicted in Figures S11 **a-d**, a reduction in the effective detection target area results in fewer sampling pixels, which, in turn, leads to a marked decline in spectral measurement precision and a notable degradation in spectral peak resolution. However, the expansion of sampling pixel count results in an

exponential increase in computational time for spectrum calculations. This is primarily due to a significant rise in both the number of MLE sets and the elements of discrete spectra vectors in the MLR solving model. Herein, we quantified the truncation effect of the diffraction pattern by the finite detector array size in spectrum measurement, as plotted in Fig. S11 **e**. It's evident that when the number of truncation pixels exceeds 1000, the enhancement in spectral resolution becomes less pronounced, while the computational cost significantly increases. To strike the balance between the spectrum measurement resolution and the computational cost, here we select 1024 pixels as the optimal sensor array size, providing a 1nm resolution, as demonstrated in Fig. S11 **f**.

To sum up, the camera's nonlinearities have several key effects on the quality of diffraction recording, thereby impacting the performance of recovered spectrum, as discussed in detail in the following.

1) Quantum efficiency (QE) nonlinearity

The QE refers to the detector's ability to efficiently convert incoming photons of broadband light into measurable electrical signals. In the proposed spectrometer, the QE of the detector is a critical factor in determining the spectrometer's overall performance.

- Firstly, the spectral response bandwidth of the spectrometer is predominantly limited by the QE of the detector.
- Secondly, the QE nonlinearity introduces inaccuracies in the power intensity of spectral measurements. These inaccuracies can be corrected by calibrating the detector's QE.
- Thirdly, a high-QE detector has a broader dynamic range, allows to capture higher-SNR diffraction signals, and thus can improve the quality of the spectra measurements.

2) ADC nonlinearity

The ADC nonlinearity in detector refers to deviations from a perfect linear response in the process of converting analog signals into digital values. This nonlinearity introduces errors in the digital representation of the analog signal and affects accuracy of the diffraction intensity. The ADC nonlinearity also introduces inaccuracies in the measurement of spectral power intensity. Moreover, different from the QE nonlinearity, these inaccuracies resulted from the ADC nonlinearity cannot be corrected. Good news is that the performance of the CCD/CMOS sensor device has seen substantial improvement, with the ADC nonlinearity typically being reduced to less than 5% across the full QE bandwidth.

3) Saturation and clipping

The saturation and shadow clipping effects lead to a decrease in the SNR of the sampled diffraction signals. This is because most of the photon energy is concentrated within the central diffraction orders, making them prone to saturation, while the higher-order

diffracted photons are much weaker and more susceptible to noise-induced blurring. As a result, these effects diminish the quality of the recovered spectra. In this work, we use a filter to remove the central fringe saturations to better utilize the ADC dynamic range of the detector.

S5 Spectral resolution with temporal decoherence of the reference diffraction I_m

As discussed in the main text, the resolution of peak separation of the bimodal spectrum degenerates from the decoherence of the quasi-monochromatic diffraction which is used to generate the PSFs over full spectrum range. This is caused by the wavelength-multiplexing of diffraction distributions of different spectral components, as described in Eq. S6. The better monochromaticity of quasi-monochromatic diffraction, the lower level of the multiplexing effect, which makes the higher resolution of spectral peak separation.

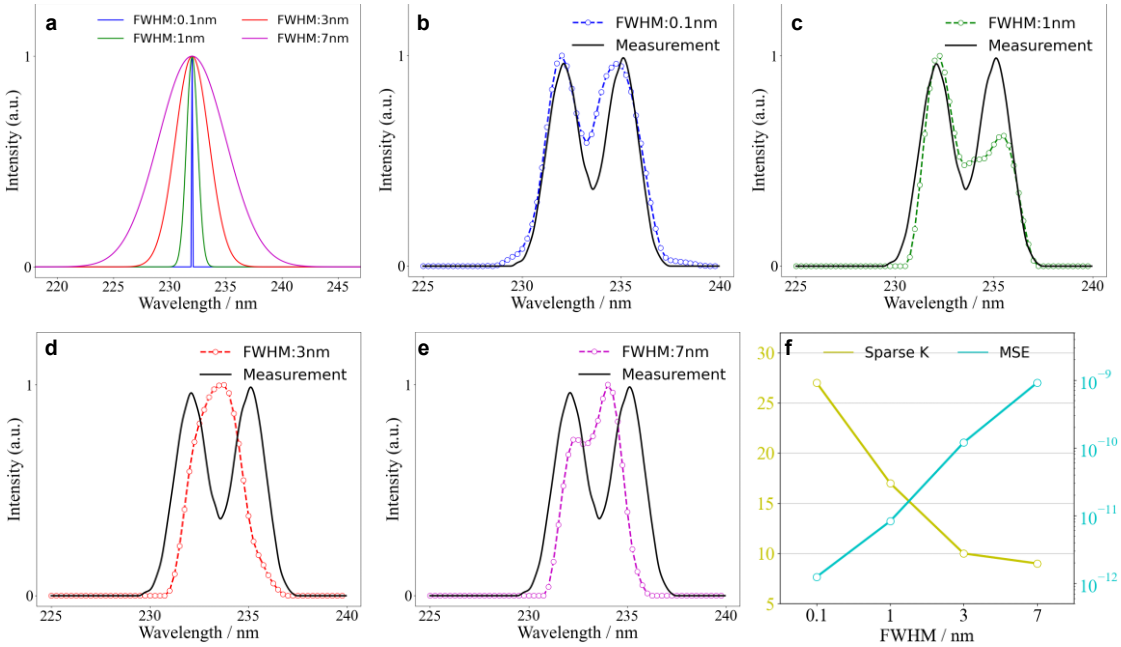

Figure S12 Simulated resolution performance with increased temporal decoherence of pre-captured diffraction. **a**， the simulated FWHMs of radiation for diffractions with different levels of decoherence. **b-d**, reconstructions using different pre-captured diffractions with 0.1nm, 1nm, 3nm, and 7nm FWHM, respectively. **f**, total number of the calculated spectrum discrete and the prediction MSE corresponding to the measurements in **b-d**, respectively.

To illustrate the temporal decoherence of pre-captured I_m in resolution, we have carried out simulations for the measurement of a bimodal spectrum at a 3nm separation from the broadband diffraction corresponding to the measured spectrum, with a set of pre-captured diffractions illuminated from varying levels of FWHMs (0.1nm, 1nm, 3nm, and 7nm) as the input data, respectively, as shown in Fig. S12**a**. The reconstructions have been simulated via the proposed spectrum measurement workflow as detailed in **S2**. For the reference diffraction illuminated with a FWHM of 0.1nm, the peaks of the measured spectrum can be clearly distinguished and with high alignment with the ground truth (Fig. S12 **b**). With the FWHM increasing, the reconstructed resolution begins to break down (Fig. S12 **c**-**e**). Seeing that the peaks of the bimodal spectrum of 3nm are separated successfully for the reference diffraction illuminated with FWHMs less than 1nm, which match well with the experimental results (as demonstrated in the Figure 3**c**, and 3**d** in the main text). Meanwhile, we have monitored

the number of solved discrete power spectrum counts and the MSE in prediction by solving Eq. S13, shown in Fig. S12 **e**. Seeing that the number of solved power spectrum counts decreases with the increase of FWHM, whereas the MSE increases simultaneously.

S6 Experimental set-up of the broadband CDI

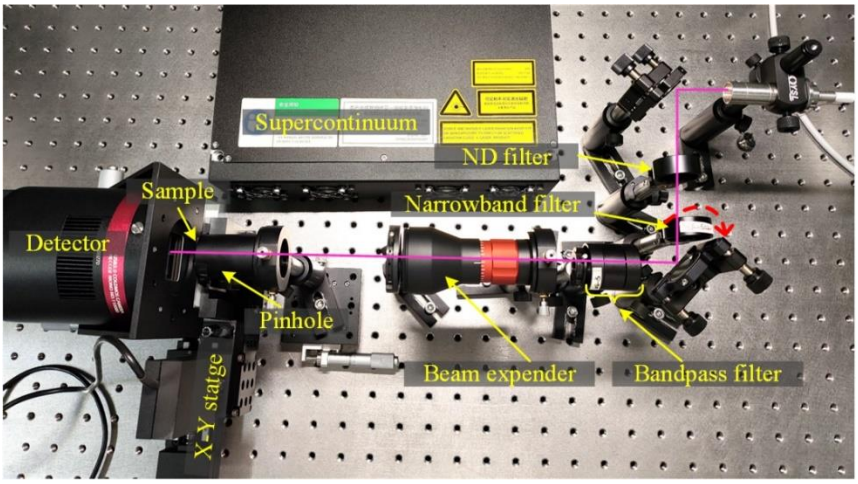

Figure S13 Schematic of broadband CDI setup. we use a 600 nm short pass filter to select a broadband spectrum (YSL Photonics SC-5) from the supercontinuum source. A 90° Flip narrowband filter at 532nm (Thorlabs FL532-3) is settled on the optical path to generate a quasi-monochromatic radiation. A pinhole with 100μm in diameter (Thorlabs P100K) is placed in front of the Siemens star resolution target (Thorlabs R1L1S1N) to filter the radiation to a plane wave with 100μm in diameter. A CMOS detector (QHY268M) is placed behind the sample at 30mm to record the diffractions. The sample is mounted on a X-Y stage (Thorlabs MTS25/M-Z8).

S7 Monochromatization from a broadband diffraction

This section describes how we monochromatize the broadband diffraction from an unknown spectrum intensity. As we have mentioned in **S1**, the wavelength-dependent scaling and weighting spectrum of copies of the pre-captured coherent diffraction pattern is perfectly suited for a matrix-vector product. As referred to Julius's previous work on numerical monochromatization of the broadband diffraction pattern, a monochromatized diffraction pattern can be retrieved based on a regularized inversion of a matrix that depends only on the spectrum of the diffracted radiation Defining the monochromatic pattern as a vector $\mathbf{m}$, the broadband diffraction pattern as vector $\mathbf{b}$ and the scaling matrix as $\mathbf{C}$, Eq. S8 can be rewritten for simplicity as:

$$\mathbf{b} = \mathbf{C}\mathbf{m} \tag{S16}$$

where $\mathbf{C}$ is regarded as containing the copies of PSF in Eq. S7 times a corresponding power spectrum profile. Eq. S16 maps a point in $\mathbf{m}$ to the profiles of power spectrum in $\mathbf{b}$. For a 2D diffraction pattern, C is a 4D tensor in shape. Note that matrix $\mathbf{C}$ is fully determined by only the spectrum of illumination system and the size of detector. in 1D case of $\mathbf{C}$ can be calculated as follows:

$$C_{n,j} = \sum_{\Lambda}\left[\min\left\{j, \frac{\lambda}{\lambda_m}n\right\} - \max\left\{j-1, \frac{\lambda}{\lambda_m}(n-1)\right\}\right]\frac{\omega(\lambda)\lambda_m}{\lambda} \tag{S17}$$

where

$$N = \left\{n : (j-1)\min\left\{\frac{\lambda_m}{\lambda}\right\} < n < j\left(\max\left\{\frac{\lambda_m}{\lambda+\lambda_m}\right\}\right)\right\}$$

$$\Lambda = \left\{\lambda : \frac{j-1}{n} < \frac{\lambda}{\lambda_m} < \frac{j}{n-1}\right\}$$

Since the matrix $\mathbf{C}$ is calculated from the measured spectrum $\omega(\lambda)$ combined with $\mathbf{b}$ and $\mathbf{m}$. The monochromatization of a broadband diffraction pattern can be reduced to the inversion of matrix $\mathbf{C}$ in Eq. S16. As the inversion is extremely sensitive to noise, which is generally unsolvable by ordinary noniterative methods. To mitigate this problem, a regularization method of BiCGStab scheme is performed to reconstruct the monochromatized diffraction[9,10]. BICGStab is performed with two additional constraints in this work: non-negativity of $\boldsymbol{m}_k$ (diffracted photon counts should not be negative) and a support constraint on the initial guess of $\boldsymbol{m}_0$ set to the measured broadband pattern $\mathbf{b}$. These constraints help to prevent overfitting and further improve the regularizing power of the method.

Besides, there is a spectral deviation between the power spectrum of the original source radiation $S(\lambda)$ and the aftermost power spectrum of the diffraction pattern $\omega(\lambda)$ on the detector, since the transmittance of the sample $T(\lambda)$ or the QE of the detector $QE(\lambda)$ is not constant over the source bandwidth, as

$$\omega(\lambda) = S(\lambda)T(\lambda)QE(\lambda) \tag{S18}$$

It should be mentioned that only if all these power spectrum profiles are measured precisely, Eq. S18 can be executed with satisfactory. Yet, in most practical applications, the aftermost power spectrum $\omega(\lambda)$ is generally very difficult to be measured, which brings the limitation on monochromatization of ultra-broadband diffraction applications. Our proposed spectrometer can be successfully used to tackle such instabilities, from which the aftermost power spectrum $\omega(\lambda)$ can be straightforwardly reconstructed, as detailed in S2. By performing the numerical BiCGStab algorithm to monochromatize the broadband diffraction pattern applying with the proposed spectrum reconstruction method, a monochromatized diffraction pattern can be successfully retrieved without any requirement of *prior* spectra of broadband illumination, detector QE or sample's transmittance.

S8 Spectral resolution with the wavelength λ_m of the pre-captured coherent diffraction I_m

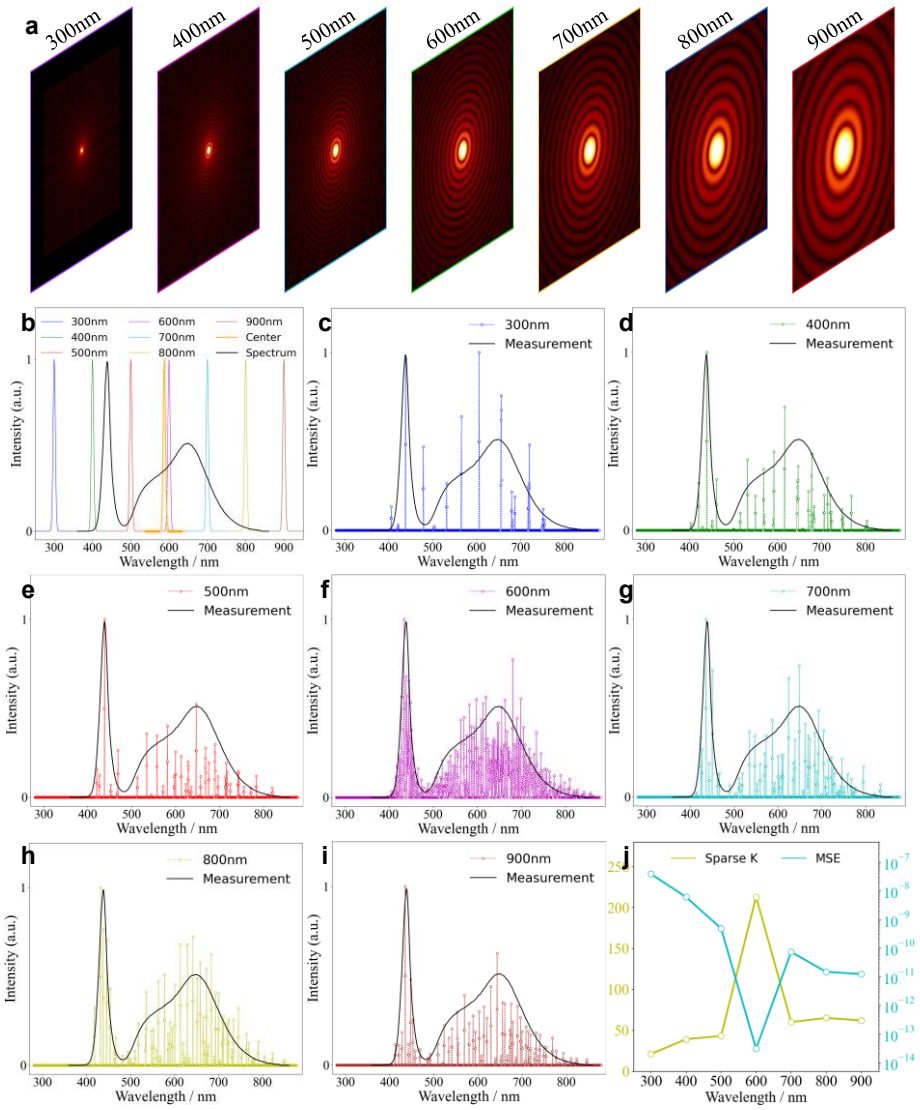

Figure S14 Simulated resolution performance with the wavelength λ_m of the reference diffraction I_m **a**, the simulated pre-captured diffraction pattern with different radiation of spectrum from 300nm to 900nm by 100nm interval, respectively. **b**, the broadband spectrum in simulation and the quasi-monochromatic spectrums corresponding to Fig. S14 **a**, orange dotted line plots the mass of the center of the broadband spectrum. **c-i**, reconstructions using different pre-captured diffractions in **Fig.** S14 **a** at wavelengths in Fig. S14 **b**, respectively. **j**, total number of the calculated spectrum discrete and the prediction MSE corresponding to the measurements in Fig. S14 **c** - Fig. S14 **i**, respectively.

Relating to our computational strategy, as detailed in section S2, to reconstruct the full spectrum from the corresponding single-shot broadband diffraction I_B, we used a PSF mapping scheme to generate n slices of wavelength-dependent quasi-monochromatic diffraction components by a uniform spectrum interval $\delta\lambda$ over full spectrum range from only one shot of pre-captured coherent diffraction I_m at a wavelength λ_m. As described in Eq. S7, the PSF mapping scheme is performed by scaling the reference

diffraction I_m with a wavelength-dependent factor λ_i/λ_m. Thus, an interpolation approach is required to be implemented on the PSFs to match with the broadband diffraction I_B with the same pixel size, which may introduce interpolation errors to the reconstructions. It is obvious that the level of interpolation errors is associated with the wavelength-dependent scaling factors, the values of λ_i/λ_m closer to 1, the smaller the interpolation errors. Thus, the choice of wavelength λ_m should better be around of the mass of the center of the broadband spectrum to suppress the interpolation errors in PSF mapping.

To illustrate the interpolation error of PSF mapping in reconstructed resolution, we have carried out simulations for the measurement of an ultra-broadband spectrum from 350nm to 850nm (black line in Fig. S14 **b**) with a series of pre-captured quasi-monochromatic diffractions at wavelengths from 300 nm to 900 nm by 100nm interval, respectively, as shown in Fig. S12 **a**, and the corresponding spectrum distributes in Fig. S14 **b**. Additionally, we calculated the weighted spectrum center of the broadband spectrum at 580 nm, as plotted with orange dotted line in Fig. S14 **b**. The calculated discrete results are plotted in Fig. S14 **c**- Fig. S14 **i**, respectively. Simulations shows that the results calculated from the pre-captured diffraction at a 600 nm wavelength, which is closest to 580nm, have the best resolution in measurement. With the wavelength of the pre-captured diffraction being father from the weighted spectrum center of the broadband spectrum, the reconstructed resolution begins to break down. Meanwhile, we have monitored the number of solved discrete power spectrum counts and the MSE in prediction by solving Eq. S13, shown in Fig. S14 **j**. Seeing that the number of solved power spectrum counts increases with the wavelength of the pre-captured diffraction close to the weighted spectrum center of the broadband spectrum, whereas the MSE decreases simultaneously.

References

1 Ioseph W. Goodman. *Introduction to Fourier Optics*. 4th ed. Roberts and Company Publishers, 2005.

2 Wang C, Xu Z, Liu H, Wang Y, Wang J, Tai R. Background noise removal in x-ray ptychography. *Appl Opt* 2017; **56**: 2099.

3 Gonzalez RC, Woods RE, Eddins SL. *Digital Image Processing Using MATLAB*. 3rd editio. Gatesmark Publishing, 2020.

4 Xu Y, Pei Y, Dong F. An adaptive Tikhonov regularization parameter choice method for electrical resistance tomography. *Flow Meas Instrum* 2016; **50**: 1–12.

5 Golub GH, Heath M, Wahba G. Generalized cross-validation as a method for choosing a good ridge parameter. *Technometrics* 1979; **21**: 215–223.

6 Hasinoff SW, Durand F, Freeman WT. Noise-optimal capture for high dynamic range photography. In: *2010 IEEE Computer Society Conference on Computer Vision and Pattern Recognition*. IEEE, 2010, pp 553–560.

7 Healey GE, Kondepudy R. Radiometric CCD Camera Calibration and Noise Estimation. *IEEE Trans PAlTERN Anal Mach Intell* 1994; **16**.

8 Wang C, Xu Z, Liu H, Wang Y, Wang J, Tai R. Background noise removal in x-ray ptychography. *Appl Opt* 2017; **56**: 2099–2111.

9 van der Vorst HA. Bi-CGSTAB: A Fast and Smoothly Converging Variant of Bi-CG for the Solution of Nonsymmetric Linear Systems. *SIAM J Sci Stat Comput* 1992; **13**: 631–644.

10 Tibshirani R. Regression Shrinkage and Selection via the Lasso. *J R Stat Soc Ser B* 1996; **58**: 267–288.